INVESTIGATION OF TIDAL-SEISMIC RESONANCE USING 3-D BOUNDARY ELEMENT METHOD

by

Yuan Tian

A dissertation submitted to the Department of Earth and Atmospheric Sciences,
College of Natural Sciences and Mathematics
in partial fulfillment of the requirements for the degree of

DOCTOR OF PHILOSOPHY

in Geophysics

Chair of Committee: Yingcai Zheng

Committee Member: Hua-Wei Zhou

Committee Member: John Suppe

Committee Member: Walter Kiefer

University of Houston

May 2020

ACKNOWLEDGMENTS

My special thanks go to my advisor, Dr. Yingcai Zheng, for his guidance and support throughout this endeavor. He gave me the most detailed guidance that nobody else in the world could give. I am amazed by his intelligence and creativity, and I benefited a lot from his insights and ideas. He has been a great role model of being a truthful and accurate scientist. I think I will remember these traits for my entire career. My sincerest appreciation goes to Dr. Hua-Wei Zhou for his help on encouraging my research. His advice on my research helped me set my career goal. The wisdom coming from his thoughts is a treasury for me. I am grateful for getting advice from Dr. John Suppe on my research; his insightful comments on my research presentation helped me realize the meaning of my research and helped me continue doing better research. I am thankful for having Dr. Walter Kiefer on my committee, the professional advice from this renowned planetary scientist has helped me grow as a better planetary researcher. I feel really lucky to be in the same research group with Dr. Hao Hu, who is very knowledgeable and experienced. I received his help for specific and complicated coding and with the overall structure of the papers. Without his help, I cannot imagine how much harder my research would be. I also want to thank all the people in our group for their technical efforts and suggestions. I'm grateful to work with all the members of UH Xfrac group; I had lots of helpful research discussion with Jiaxuan Li, Yinshuai Ding and Yuesu Jin; David Li and Paige Given helped me improve my English writing on my papers. I thank all the faculty and students of the EAS department for their kindness and support. Last but certainly not least, my deepest gratitude goes to my parents for their constant encouragement and total support, they always picked me up when I was at the lowest point. I am so blessed for being their son.

ABSTRACT

In this dissertation, I theorize and propose a new astronomical phenomenon, called tidal-seismic resonance for a solid planet-moon system. To fully study the resonance, I develop an open-source modeling code, AstroSeis, to model seismic waves in a planet excited by the tidal force of the orbiting moon.

Tidal seismic resonance happens when a tidal force frequency of an orbiting moon matches a free-oscillation frequency of the planet. Here I show that when the moon is close to the planet, the tidal-seismic resonance can cause large-amplitude seismic waves, which can change the shape of the planet and in turn, exert a negative torque on the moon causing it to fall rapidly toward the planet. I present this main finding in the last chapter, Chapter 6. However, I present the necessary preliminaries to understand this major conclusion and development of the modeling tool in the preceding chapters.

After introductory materials in Chapter 1, I give a detailed analysis of tidal forces for a co-rotating planet-moon system in Chapter 2. In Chapter 3, I present the basics and preliminaries of the normal modes and free-oscillation frequencies of a solid planet.

I present my newly developed seismic modeling tool, AstroSeis, in Chapter 4. This tool is a 3D seismic wavefield modeling code using the boundary element method. It can handle arbitrary surface topography of a planet or an asteroid and allow for a liquid core. Because AstroSeis is formulated in the frequency domain, it is particularly suited to model seismic wavefield caused by long-term forcing such as periodical tidal forces. I also show AstroSeis could be used to study interior and surface processes of planets and asteroids.

In Chapter 5, I use the seismic displacement computed by AstroSeis to numerically calculate the traditional tidal torque. The tidal torque is important because it causes the orbital decay of the orbiting moon.

The tidal-seismic resonance could also be an important mechanism in other settings such as in the planetary accretion process. On the other hand, AstroSeis can be used to study a wide range of planetary phenomena in particular planetary/asteroid surface processes due to seismic shaking.

TABLE OF CONTENTS

ACKNOWLEDGMENTS ..... **ii**

ABSTRACT ..... **iii**

TABLE OF CONTENTS ..... **v**

LIST OF FIGURES ..... **viii**

LIST OF TABLES ..... **xiii**

Chapter 1 Introduction **1**

1.1 Idea of tidal-seismic resonance **1**

1.2 Seismic wavefield modeling for asteroid and small bodies **2**

1.3 Future research topics **4**

1.3.1 Understanding asteroid surface processes 4

1.3.2 Potential role of tidal-seismic resonance in planetary accretion 5

1.4 Summary **5**

Chapter 2 Planet deformation by tidal force **7**

2.1 Tidal force and tidal potential **7**

2.2 Tidal deformation – equation of motion **9**

2.2.1 Planet with self-gravitation 9

2.2.2 Planet without self-gravitation 11

2.3 Love numbers **13**

2.3.1 Self-gravitation case 13

2.3.2 Non self-gravitation case 15

2.4 Summary **15**

Chapter 3 Free oscillations of a planet and normal mode frequencies 16

3.1 Governing equations and boundary conditions 16

3.2 Eigen-frequencies and normal modes 20

3.2.1 Toroidal modes 20

3.2.2 Spheroidal modes 21

3.3 Normalization of normal modes 22

3.4 Normal mode summation for making synthetic seismograms 25

3.5 Summary 28

Chapter 4 Boundary element method for irregular bodies seismic modeling 29

4.1 Method and boundary integral equations 29

4.1.1 A solid asteroid with topography 29

4.1.2 Solid body with a liquid core 32

4.2 Benchmark of BEM 35

4.2.1 Benchmark example 1 - Homogenous solid sphere with a single force source 35

4.2.2 Benchmark example 2- Homogenous solid sphere with explosion source 40

4.2.3 Benchmark example 3 - Solid sphere with a liquid core 42

4.3 Numerical examples 46

4.3.1 Shifted-core model 46

4.3.2 Seismic modeling for Phobos 48

4.3.3 Seismic exploration of Phobos 49

4.4 Incident field from tidal force 51

4.5 Summary 52

Chapter 5 Tidal torque and orbital decay rate 53

5.1 Methods 53

5.1.1 Numerical torque from BEM 53

5.1.2 Analytical torque from Love number 54

5.2 Comparison between analytical torque and BEM numerical torque 55

5.3 Summary 55

Chapter 6 Tidal-seismic resonance 57

6.1 Model setup 57

6.2 When tidal-seismic resonance can happen 58

6.3 Effect of tidal-seismic resonance 59

6.3.1 Tidal-seismic resonance at low orbits 59

6.3.2 Topography induced tidal-seismic resonance 61

6.4 Mars-Phobos system 64

6.5 Summary 65

Appendix 66

Analytical non self-gravitation Love number calculation Mathematica script 66

Bibliography 72

LIST OF FIGURES

Figure 1 Love numbers of different λ/μ values. The asymptotic value for infinite λ/μ is plotted in red horizontal line, the vertical axis is the Love number h_2.....14

Figure 2 The toroidal modes frequencies at different angular orders. The planet has 2000km in radius, the compressional wave velocity of the planet is $vp = 3$ km/s, the shear wave velocity $vs = 1.2$ km/s and the density of the planet is 2840 kg/m^3.....21

Figure 3 The spheroidal modes frequencies at different angular orders. The planet has 2000km in radius, the compressional wave velocity of the planet is $vp = 3$ km/s, the shear wave velocity $vs = 1.2$ km/s and the density of the planet is 2840 kg/m^3.....22

Figure 4 Geometry used in BEM. (a) A solid asteroid. The domain in gray is the solid medium Ω. S is the surface of this domain. We partition the surface into M small triangles. Σ_I and $\Sigma_{I'}$ are boundary elements on S with indices I and I', respectively. x_I is the collocation point on the element Σ_I which is defined as the center of the inscribed circle on Σ_I. $x0$ is the location of the source. n is the surface normal on S. (b) A solid body with a liquid core schematic. Ω_1 is representing the solid medium which is the space in gray. Ω_2 is representing the liquid medium which is the space in blue. J and J' are element indices on S_2.....32

Figure 5. A Homogenous model with a single-force source. (a) The source and receivers are on the equatorial plane. The solid body is 20 km in radius. We placed the source (indicated by a red star) at depth of 10 km, 180° in longitude and 0° in latitude. The direction of the force is given by the yellow arrow. All the receivers are placed on the equator, spaced at an interval of 5°. (b) 3D view of the boundary mesh. The red star is the source location. The blue circle in the middle is the equator. The yellow line is the axis through the poles. 37

Figure 6 Seismic displacement (vertical component) waveform of the model in Figure 5 using two different methods: BEM and normal modes summation, for a single force source. (a) Wiggle-to-wiggle comparison of seismic waveforms due to a single force source shown in Figure 5. (b) A common source gather by BEM; (c) Common source gather by the normal mode summation method. 39

Figure 7 An explosion source in a homogeneous model. (a) The source and receivers are on the equatorial plane. The solid body is 20km in radius. We placed the source indicated by a red star at depth of 10km, 180° in longitude and 0° in latitude (on the equator plane). All the receivers are also placed on the equator, spaced at an interval of 5°. (b) 3D view of the boundary mesh. The red star is the location of the source. The orange circle is the equator. The red line is the axis through the poles. 41

Figure 8 Seismic displacement fields (vertical component) for the model in Figure 7 computed by BEM and the normal mode summation for an explosion source. (a) Wiggle-to-wiggle comparison of seismic waveforms due to an explosion source shown in Figure 7. (b) Common source gather computed by BEM; (c) Common source gather by the normal mode summation method. 42

Figure 9 A solid sphere with a liquid core model with an explosion source. (a) The source (red star) and receivers (orange triangles) shown on the equatorial plane. The solid body is 20km in radius. The liquid core is 10km in radius. We placed the source at depth of 4km, 180° in longitude and 0° in latitude (on the equator plane). All the receivers are on the equator, spaced at an interval of 5°. (b) 3D view of the boundary mesh. The red star is the location of the source. The orange circle is the equator. The red line is the axis through the poles. 44

Figure 10 Seismic displacement (vertical component) comparison between BEM and DSM for an explosion source. (a) Wiggle-to-wiggle comparison of seismic waveforms (BEM versus DSM). (b) Common source gather by BEM; (c) Common source gather by DSM (Kawai et al., 2006).....45

Figure 11 The seismic wavefield (vertical displacement) in a solid sphere with a shifted liquid core. (a) The mesh of a solid sphere with a shifted liquid core to calculate seismic displacement wavefield. The core is shifted along the y direction by 2km. The explosion source is given as an identity matrix. The source location is indicted by a red star, at a depth of 4km, 180° in longitude, and 0° in latitude (on the equator plane). All the receivers are placed on the equator at an interval of 5°. In this solid medium, we set the compressional wave velocity $vp = 6\ km/s$ and the shear wave velocity $vs = 3$ km/s, the density $\rho = 3000\ kg/m^3$; in the liquid medium, we set compressional wave velocity $vp = 8000m/s$, density $\rho = 4000\ kg/m^3$. (b) Common source gather for the shifted-core model in (a). (c) Common source gather from a solid sphere with a centered liquid core (i.e., no shift).....47

Figure 12. Seismic wavefield in Phobos. (a) The topography model of Phobos with the surface mesh. We define the positive x-axis is 0° in longitude, the positive y-axis is 90° in longitude. The source location is indicated by a blue star, at depth of 4km, 180° in longitude and 0° in latitude (on the equatorial plane). All the receivers are placed on the approximated equator with an interval of 5°. In this model, I set the compressional wave velocity $vp = 3\ km/s$ and the shear wave velocity $vs = 1$ km/s, the density $\rho = 1880\ kg/m^3$. And the explosion source is given as an identity matrix. (b) Common source gather from the model shown in (a). (c) Common source gather from an elastic sphere with 10.9km in radius. 49

Figure 13 Snapshot of modeled seismic wavefield patterns on the surface of Phobos at different frequencies. The value shown (red/blue color) is the signed square root of real part of the seismic displacement to enhance contrast for visualization. 50

Figure 14. Comparison of analytical torque and numerical torque (based on the boundary element modeling, see equation (5.1) for different orbital radii and Q values. The analytical torque is computed using equation (2.21) and (5.3) with $h_2 = 0.5877$. R_{pl} is the planet's radius equal to 2000 km. 56

Figure 15. Tidal force and planet normal mode frequencies for model-1. The solid lines are tidal force frequencies calculated for a point on the planet equator. The vertical dashed lines are the planet free-oscillation frequencies for the spheroidal $_0S_n$ normal modes (n=2, 3, 4, …). The tidal-seismic resonance occurs when tidal force frequencies intersect the planet free oscillation frequencies at the red circles. 59

Figure 16. Calculated moon orbital decay rates at different orbital radii and for different Q values for model-1. The horizontal axis is the radius of the moon orbit. The radius of the planet Rpl is 2×106m. I also label excited normal modes, $0Sn, n > 2$, expected to be seen for the tidal-seismic resonance. 61

Figure 17. A model with topography (model-2) for the planet. I have exaggerated the plotting of the topography by 20 times. Colors indicate topography relative to the mean radius of the planet with size given in meters. The thick red line is the equator. The blue vertical thick line is the axis through the poles. 62

Figure 18. The derivative of the orbital decay rate with respect to the orbital radius for (a) model-2 with topography and (b) model-1 with no topography. Here, fn is the frequency of the normal mode $0Sn$. A dashed line shows the orbit whose orbital frequency is

fn/m, where n and m are integers and labeled accordingly next to the dashed line. The radius of the planet Rpl is 2×10^6m. 64

LIST OF TABLES

Table 1 Numerical values of Love number for different λ/μ ratios. 14

Chapter 1 Introduction

I will first introduce the idea of tidal-seismic resonance (Tian and Zheng, 2019) and the history and development of other coupling effects between tidal force and seismic wavefields in the planet. In order to study the tidal-seismic resonance, I need to model seismic fields in a planet with topography. To do so, I created a 3D modeling code, AstroSeis, for the modeling and I will differentiate my approach from other existing seismic modeling methods. Finally, I will briefly discuss future potential research topics and the application of my seismic modeling code in understanding other planetary processes.

1.1 Idea of tidal-seismic resonance

Darwin (1898a) first proposed the idea of a gravity-seismic coupled resonance of a fluid planet to explain the Moon formation. He argued that the violent vibration of the planet at resonance "*... shook the planet to pieces, detaching huge fragments which ultimately were consolidated into the Moon."* While Darwin's idea of moon formation theory has been largely discarded, very little work has been done to investigate possible consequences of the tidal-seismic resonance for a planet-moon system, in particular for a solid planet.

Tidal force frequencies are usually out of the range of planet free oscillation (or normal mode) frequencies. Even the tidal force of the very fast orbiting Phobos around Mars does not produce a significant effect on the Martian free oscillation in the current orbital configuration (Lognonné *et al.*, 2000).

However, in some cases, tidal force frequencies can intrude into the frequency range of the planet's normal modes. For example, the tidal force on a rapidly rotating planet can excite the normal modes of the planet (Braviner and Ogilvie, 2014a; b; Barker *et al.*, 2016). Interaction between Saturn's ring and Saturn can excite the acoustic free oscillation of Saturn

(Marley, 1991; Marley and Porco, 1993; Marley, 2014). Fuller (2014) used the tidal force to detect the acoustic free oscillation frequencies by observing density waves in the Saturn ring. Furthermore, Fuller *et al.* (2016) also studied the resonance between tidal force and the acoustic free oscillation of gas giants (e.g., Saturn and Jupiter) which could change the migration of the moons.

My goal here is to perform theoretical and numerical analysis to investigate first-order effects of tidal-seismic resonance for a solid planet.

1.2 Seismic wavefield modeling for asteroid and small bodies

To model seismic waves in an asteroid, we need to address two issues. First, we must be able to consider surface topography because asteroids are irregular in geometry and topography can influence seismic waves significantly. Secondly, some seismic sources are periodic and long in duration such as the tidal force, we need the ability to model in the frequency domain and to incorporate a frequency-dependent Q. For these reasons, we develop a 3D frequency-domain elastic boundary element method (BEM). In addition, my BEM can also include a liquid core for a geologically differentiated body.

There are many widely used numerical methods to model seismic wavefields in Earth or other celestial bodies. For a 1-D spherical model, we can use the normal mode method (Ben-Menahem and Singh, 1981; Dahlen and Tromp, 1998; Aki and Richards, 2002). This method is the exact solution to model seismic wavefields. The package, MINEOS (Masters *et al.*, 2011), is a publicly available software used to model normal mode synthetic seismograms. However, its ability to model waves higher than 166mHz is limited for the Earth. The direct solution method (DSM) (Cummins *et al.*, 1994a; Cummins *et al.*, 1994b; Geller and Takeuchi, 1995; Takeuchi *et al.*, 1996; Kawai *et al.*, 2006) is also a 1-D model based code which can compute high frequency (e.g. > 1 Hz) synthetic data. In principle, DSM can also

handle irregular topographies (Geller and Ohminato, 1994). However, the code released by Takeuchi (Kawai *et al.*, 2006) can only handle 1-D spherical models. Other numerical methods can model seismic wavefields in a more complex model, for example, the finite difference method (FD) (Boore, 1972; Fang *et al.*, 2014; Zhan *et al.*, 2014). FD is known to have difficulties in modeling wave scattering by irregular topographies. Recent progress by Zhang *et al.* (2012) added the topography modeling capabilities at local scales however its application in global scales remains to be demonstrated. The spectral element method (SEM) (Komatitsch and Tromp, 1999) is a powerful numerical method in modeling waves in 3-D Earth. However, its domain meshing will need specialized software and training. Both FD and SEM are implemented in the space-time domain by discretizing 3-D space into small grids and time into small marching steps. A frequency-dependent Q is not straightforward to be incorporated in FD and SEM. The grid dispersion can be another issue if the modeled seismic field is long in time duration (e.g., due to cyclic tidal forces). To avoid the grid dispersion in FD and SEM, usually very fine grids and a small time-step should be used. However, this method is computationally expensive. On the other hand, if the source location is changed, we need to compute the wavefield again for FD and FEM. However, it is not true for BEM as it can simultaneously handle multiple sources with little added computation. Note that there is no 'best' modeling method universally. Each modeling method, under certain circumstances, can be more or less advantageous than others, depending on the objectives.

My BEM is based on the boundary integral equation (e.g., Sánchez-Sesma and Campillo, 1991; Ge *et al.*, 2005; Ge and Chen, 2008; Zheng *et al.*, 2016). BEM only discretizes the model on the boundaries and interfaces, which represents a dimension reduction by one. Therefore, BEM can be less computationally intensive than the other 3-D numerical seismic modeling method (Stamos and Beskos, 1996; Chaillat *et al.*, 2009). Here, I present the BEM

method and the associated code to model seismic wavefield in asteroids and small bodies in space. The BEM code is named AstroSeis. It is easy to set up and use in MATLAB.

1.3 Future research topics

Building upon the current development in this thesis, I anticipate a new set of analyses can be done in the future.

1.3.1 Understanding asteroid surface processes

The open source code, AstroSeis, developed in this thesis will be very useful in probing the interior and understanding the surface features of an asteroid in a future asteroid mission with or without a seismological payload. Asteroids and meteorites provide clues to understanding the formation of planetesimals in the solar system. The internal elastic structure of asteroids is poorly constrained (Johansen *et al.*, 2015; Walsh, 2018). Murdoch *et al.* (2017) showed that the passive seismic activity on the asteroid, Didymoon, could be used to distinguish different proposed internal models. On the other hand, many astronomical/planetary processes are related to seismic waves or shaking. For example, seismic shaking can reshape an asteroid surface because they can exert large stresses exceeding the low gravity (Asphaug *et al.*, 1996). AstroSeis can be used to analyze the asteroid Bennu's OSIRIS-REx images (DellaGiustina *et al.*, 2019) and lidar for clues in features like run-outs, slopes, particle sorting to infer internal compositions and physical properties. We can also examine the resurfacing event caused by the impact on the Ryugu asteroid (Arakawa *et al.*, 2020). Similar work can be done for the future Martian Moon eXploration (MMX) mission to Phobos. Future seismic exploration of asteroids should consider fiber optical sensing. An optical fiber

cast out from a "fishing pole" type device can wrap around a small asteroid to continuously monitor the vibration.

AstroSeis can also be used to study planetary processes. For example, the antipodal geological disruption on Mercury has been hypothesized to be formed by seismic focusing from the Caloris basin impact (Schultz and Gault, 1975; Lu *et al.*, 2011). A second potential AstroSeis application example is the ongoing InSight mission, which is about the seismic exploration of Mars where several prominent topographic features are around the InSight seismometer (Banerdt *et al.*, 2020; Giardini *et al.*, 2020; Lognonné *et al.*, 2020).

1.3.2 Potential role of tidal-seismic resonance in planetary accretion

The tidal-seismic resonance is more likely to occur for a smaller rocky planet (radius < 1000 km) than a larger planet because of the matching of seismic normal mode frequencies of the planet and possible tidal frequencies caused by an orbiting object. It can be postulated that during planetary accretion, particles swirling around the accreted portion of the planet can experience tidal-seismic resonance and rapidly fall to accelerate during the accretion process.

1.4 Summary

In this chapter, I have introduced the initial hypothesis and some development of interaction between the tidal force and the free oscillation of a plane. We propose a new phenomenon "tidal-seismic resonance" for solid planets and orbiting moons. I also introduce the importance of seismic modeling in asteroids study. I compare the advantages and limitations of the AstroSeis code that is based on the boundary element method with other seismic

modeling methods. Finally, I introduce some future applications on asteroids using the AstroSeis.

Chapter 2 Planet deformation by tidal force

In tidal-seismic resonance, tidal forces of an orbiting moon excite seismic waves in a planet. In this chapter, I will first show how to compute tidal forces for an orbiting moon around the planet. The word "tidal" was usually understood as regular and persistent alternations of rise and fall of the sea-level (Darwin, 1898b). Here, I consider the solid tides raised on the planet surface by an external gravitational field (Murray and Dermott, 1999). To describe and analyze the effect of the tidal force, it is convenient to use tidal potential.

2.1 Tidal force and tidal potential

The tidal force of the orbiting moon can be understood following Newton's law of universal gravitation. We can obtain the formula of the tidal force acceleration, **g**, at a location $\mathbf{x}'$ inside the planet:

$$\mathbf{g}(\mathbf{x}', t) = \frac{G m_{moon}}{|\mathbf{x_m} - \mathbf{x}'|^3}[\mathbf{x}_\mathrm{m}(t) - \mathbf{x}'] + \boldsymbol{f}_{cf}(\mathbf{x}', t), \tag{2.1}$$

where $\mathbf{x}_m(t)$ is the position of the moon at the time t on a circular orbit with a constant angular speed, ω_0. G is the universal gravitational constant (~ $6.674 \times 10^{-11}\ m^3 kg^{-1} s^{-2}$). m_{moon} is the mass of the moon. $\mathbf{f}_{cf}(\mathbf{x}', t)$ is the centrifugal force at $\mathbf{x}'$. We can use this formula to calculate the excitation of the seismic field for our seismic wavefield modeling later in section 4.4.

Because the gravity force acceleration $\boldsymbol{f_g}$ of the moon is the gradient of its gravitational potential $V(\mathbf{x}, t)$:

$$\boldsymbol{f_g}(\mathbf{x}, t) = -\nabla V(\mathbf{x}, t), \tag{2.2}$$

We can analyze the frequencies of the gravitational potential to observe the frequencies of tidal forces. The moon's orbital frequency is ω_0, but it can also generate other higher harmonic frequencies. To observe them, we can analyze the first term in (2.1) by looking at the moon's gravitational potential (Taylor and Margot, 2010)

$$V(\mathbf{x},t) = -\frac{Gm_m}{|\mathbf{x}_m(t)-\mathbf{x}|} = -\sum_{n=1}^{\infty} \frac{Gm_m|\mathbf{x}|^n}{r_m^{n+1}} P_n[\cos\psi(t)], \tag{2.3}$$

where P_n is n-th order Legendre polynomial, $\psi(t)$ is the angle between vectors $\mathbf{x}$ and $\mathbf{x}_m(t)$, and r_m is the radius of the moon's circular orbit along the planet's equatorial plane. For a point $\mathbf{x}$ in the planet, the gravity potential is changing with time because of the term in the Legendre polynomial, $P_n[\cos\psi(t)]$. If the orbit frequency is ω_0, $P_n[\cos\psi(t)]$ has the term $\cos(n\omega_0 t)$, whose frequency is $n\omega_0$ (n=0, 1, 2, …). Therefore, the tidal force frequencies of the moon are discrete and have higher order harmonics. We note that the centrifugal force can cancel the term $n = 1$ of the gravitational potential V. Therefore, n should start from 2, and the tidal potential is:

$$V_{tide}(\mathbf{x},t) = -\sum_{n=2}^{\infty} \frac{Gm_m|\mathbf{x}|^n}{r_m^{n+1}} P_n[\cos\psi(t)]. \tag{2.4}$$

We can truncate the angular order to any order in equation (2.4) for different purposes. We consider the case that the mass of the moon is much smaller than the planet; therefore, the center of the planet is almost the same as the center of mass of the two-body system.

2.2 Tidal deformation – equation of motion

2.2.1 Planet with self-gravitation

To derive the analytical tidal deformation, I consider a spherical planet model that is in hydrostatic equilibrium under the self-gravitation. The displacement can be obtained by solving the following equations which do not have the particle acceleration term $\ddot{\boldsymbol{u}}$ due to seismic waves:

$$\begin{aligned} -\rho\nabla V_{tide} + \nabla\cdot\sigma - \nabla(\rho\mathbf{u}\cdot\mathbf{g_0}) + \rho\nabla K + \rho\mathbf{g_0}\nabla\cdot\mathbf{u} = \mathbf{0}, \\ \nabla^2 K - 4\pi G\rho\nabla\cdot\mathbf{u} = 0, \end{aligned} \tag{2.5}$$

where $\mathbf{u}$ is the displacement field within the planet caused by the tidal force and ρ is the density. Here, V_{tide} is the tidal potential field of the moon that causes the deformation, σ is the 2nd rank elastic stress tensor field, K is the gravitational potential field caused by the density perturbation due to seismic waves, and $\mathbf{g}_0$ is the vector gravitational acceleration of the planet:

$$\mathbf{g}_0(\mathbf{r}) = \frac{4}{3}\pi G\rho\, r\boldsymbol{e_r}, \tag{2.6}$$

where $\boldsymbol{e_r}$ is the unit vector along the outward radial direction and r is the distance from the point to the center of the planet. When the moon is not too close to the planet (i.e. more than 2 times of the planet radius) we can just consider the degree-2 ($l = 2$) tidal potential in equation (2.4). The planet is spherical. It is convenient to use spherical coordinates in this study. Here, we use spherical coordinate r, θ, ϕ to write the degree-2 tidal potential:

$$V_{tide}(r,\theta,\phi) = -\frac{2Gm_m r^2}{r_m^3}\sqrt{\frac{\pi}{5}}Y_2^m(\theta,\phi), \tag{2.7}$$

where $Y_2^m(\theta,\phi)$ is degree-2 normalized spherical harmonics. We can have three components of the tidal force $\boldsymbol{g}_{tide}$ in terms of spherical coordinates:

$$g_{tide_r} = \frac{4Gm_m\rho r}{r_m^3}\sqrt{\frac{\pi}{5}}Y_2^m(\theta,\phi), \tag{2.8}$$

$$g_{tide_\theta} = \frac{2Gm_m \rho r}{r_m^3} \sqrt{\frac{\pi}{5}} \frac{\partial Y_2^m(\theta,\phi)}{\partial \theta},$$

$$g_{tide_\phi} = \frac{2Gm_m \rho r}{r_m^3} \csc(\theta) \sqrt{\frac{\pi}{5}} \frac{\partial Y_2^m(\theta,\phi)}{\partial \phi},$$

The divergence of elastic stress tensor σ can be written using two Lame' constants μ and λ:

$$\nabla \cdot \sigma = (\lambda + 2\mu)\nabla\nabla \cdot \mathbf{u} - \mu\nabla \times (\nabla \times \mathbf{u}). \tag{2.9}$$

To express displacement in spherical coordinates, we introduce three surface harmonics for spherical coordinates:

$$\boldsymbol{R_l^m}(\theta,\phi) = Y_l^m(\theta,\phi)\boldsymbol{e_r},$$

$$\boldsymbol{S_l^m}(\theta,\phi) = \frac{1}{\sqrt{l(l+1)}}\left[\frac{\partial Y_l^m(\theta,\phi)}{\partial \theta}\boldsymbol{e_\theta} + \frac{1}{\sin(\theta)}\frac{\partial Y_l^m(\theta,\phi)}{\partial \phi}\boldsymbol{e_\phi}\right], \tag{2.10}$$

$$\boldsymbol{T_l^m}(\theta,\phi) = \frac{1}{\sqrt{l(l+1)}}\left[-\frac{\partial Y_l^m(\theta,\phi)}{\partial \theta}\boldsymbol{e_\phi} + \frac{1}{\sin(\theta)}\frac{\partial Y_l^m(\theta,\phi)}{\partial \phi}\boldsymbol{e_\theta}\right].$$

We can write the seismic displacement field $\boldsymbol{u}$ in the spherical coordinate as:

$$\boldsymbol{u}(r,\theta,\phi) = U(r)\boldsymbol{R_l^m}(\theta,\phi) + V(r)\boldsymbol{S_l^m}(\theta,\phi) + W(r)\boldsymbol{T_l^m}(\theta,\phi). \tag{2.11}$$

By substituting equation (2.6), (2.8), (2.9) and (2.11) into equation (2.5), we can get four differential equations system with respect to r, θ, ϕ for angular order $l = 2$ (degree-2):

$$
\begin{aligned}
&2Ar^3\rho + \frac{4}{3}G\pi r^2\rho^2 U(r) - 10\mu U(r) - 2B\mu U(r) - 8G\pi r^2\rho^2 V(r) + 18\mu V(r) \\
&\quad + 6B\mu V(r) + r^2\rho K'(r) + 4r\mu U'(r) + 2Br\mu U'(r) - 6r\mu V'(r) \\
&\quad - 6Br\mu V'(r) + 2r^2\mu U''(r) + Br^2\mu U''(r) = 0, \\
&Ar^3\rho + r\rho K(r) - \frac{4}{3}G\pi r^2\rho^2 U(r) + 4\mu U(r) + 2B\mu U(r) - 12\mu V(r) \\
&\quad - 6B\mu V(r) + r\mu U'(r) + Br\mu U'(r) + 2r\mu V'(r) + r^2\mu V''(r) \\
&\quad = 0, \\
&-6K(r) - 8G\pi r\rho U(r) + 24G\pi r\rho V(r) + 2rK'(r) - 4G\pi r^2\rho U'(r) + r^2K''^{(r)} \\
&\quad = 0,
\end{aligned}
\tag{2.12}
$$

where A is a constant, $A = \frac{2Gm_m}{r_m^3}\sqrt{\frac{\pi}{5}}$. B is the ratio between Lame' constants, $\lambda = B\mu$. To solve equation (2.12), we need to add boundary condition to it. Because of the free surface condition, we can have zero surface traction:

$$
\begin{aligned}
&\frac{3K(a)}{a} - 4G\pi\rho U(a) + K(a) = 0, \\
&2U(a) - 6V(a) + 3aU'(a) = 0, \\
&U(a) - V(a) + aV'(a) = 0,
\end{aligned}
\tag{2.13}
$$

where a is the radius of the planet. Combining equation (2.12) and (2.13), we can numerically solve for the degree-2 radial functions, $U(r), V(r)$ and $K(r)$, in my thesis.

2.2.2 Planet without self-gravitation

When we do not consider the effect of self-gravitation, the equation of motion becomes:

$$-\rho\nabla V_{tide} + \nabla\cdot\sigma = 0. \tag{2.14}$$

With the same traction-free boundary conditions on the planet surface, we can also get the differential equations system to solve for the seismic displacement field. In the equation (2.12), we can see the terms involving $\mathbf{g}_0$ and K are due to the planet self-gravitation. These terms can be ignored if we do not consider the self-gravitation effect. A much simpler differential equation system for a non-self-gravitating planet is:

$$\begin{aligned} &2Ar^3\rho + 10\mu U(r) - 2B\mu U(r) + 18\mu V(r) + 6B\mu V(r) + 4r\mu U'(r) \\ &\quad + 2Br\mu U'(r) - 6r\mu V'(r) - 6Br\mu V'(r) + 2r^2\mu U''(r) \\ &\quad + Br^2\mu U''(r) = 0, \\ &Ar^3\rho + 4\mu U(r) + 2B\mu U(r) - 12\mu V(r) - 6B\mu V(r) + r\mu U'(r) + Br\mu U'(r) \\ &\quad + 2r\mu V'(r) + r^2\mu V''(r) = 0. \end{aligned} \tag{2.15}$$

To solve for this differential equation system, we need to also add zero surface traction condition:

$$\begin{aligned} 2U(a) - 6V(a) + 3aU'(a) = 0, \\ U(a) - V(a) + aV'(a) = 0. \end{aligned} \tag{2.16}$$

Combining equation (2.15) and (2.16), we can solve for the radial function $U(r)$ and $V(r)$. The analytical solutions for angular order $l = 2$ of (2.15) are:

$$\begin{aligned} U(a) &= C_1 a + C_2 a^3 - \frac{A(10+3B)}{35(2+B)\mu}a^3, \\ V(a) &= \sqrt{\frac{3}{2}}C_1 a + \frac{\left(7\sqrt{6}+5\sqrt{6}B\right)C_2}{6B}a^3 - \frac{\sqrt{\frac{3}{2}}A(12+5B)}{35(2+B)\mu}a^3, \end{aligned} \tag{2.17}$$

where the coefficients $C_1 = \frac{2a^2A(3+4B)}{(14+19B)\mu}$, $C_2 = -\frac{48A\left(B+B^2\right)}{35(2+B)(14+19B)\mu}$.

2.3 Love numbers

2.3.1 Self-gravitation case

The tidal Love number h_2 is defined as a ratio of the radial displacement on the solid planet surface caused by the moon's degree-2 tidal potential and the tidal height raised on a hypothetical fluid planet due to the same degree-2 tidal potential. Another tidal Love number is k_2, which is the potential Love number defined as the ratio of the additional potential produced by the deformation of the moon's degree-2 tidal potential. Assuming the moon is orbiting the planet on the planet's equatorial plane, the tidal Love number is defined as,

$$h_2 = u_r/(V_{tide}/|\mathbf{g}_0(a)|), \tag{2.18}$$

where u_r is the radial displacement on the equator caused by V_{tide} which is the degree-2 tidal potential, and $\mathbf{g}_0(a)$ is the gravitational acceleration on the planet surface.

From the solution of differential equation system (2.12) and (2.15), we get:

$$u_r = U(a)Y_2^m(\theta, \phi). \tag{2.19}$$

Taking a ratio between equation (2.19) and equation (2.7), we get:

$$\frac{u_r}{V_{tide}} = \frac{U(a)r_m^3}{2Gm_m a^2}\sqrt{\frac{5}{\pi}}. \tag{2.20}$$

Therefore, we get the Love number:

$$h_2 = \frac{2\sqrt{5\pi}}{3}\rho\frac{U(a)r_m^3}{am_m}. \tag{2.21}$$

The Love number h_2 of the planet has an analytical expression if the planet is homogeneous and incompressible ($\lambda/\mu \to \infty$) (see Love, 1911, p109):

$$h_2 = \frac{5}{2}\left(1 + \frac{19\mu}{2\rho g_0 a}\right)^{-1}, \tag{2.22}$$

where μ is the shear modulus of the planet, ρ the density of the planet, g_0 is the planet's gravity on its surface, and a is the planet's radius. This number agrees with the number from the solution of (2.12). For example, in a planet model with the compressional wave velocity

$v_p = 3$ km/s, the shear wave velocity $v_s = 1.2$ km/s and the density $\rho = 2840\ kg/m^3$, the Love number from solution of (2.12) is $h_2 = 0.483$. The analytical Love number from (2.22) is $h_2^* = 0.471$. In the following, I numerically calculate h_2 for compressible media for different λ/μ ratios when we keep μ as the same (Table 1) (Figure 1). We can see as the λ/μ ratios increase, the Love number h_2 is approaching the asymptotic value for infinite λ/μ Love number $h_2^* = 0.471$. We can conclude the proposed numerical method should be consistent with the analytical solution.

Table 1 Numerical values of Love number for different λ/μ ratios.

λ/μ	1.0	2.0	4.0	8.0	10.0
Love number (h_2)	0.511	0.494	0.484	0.478	0.476

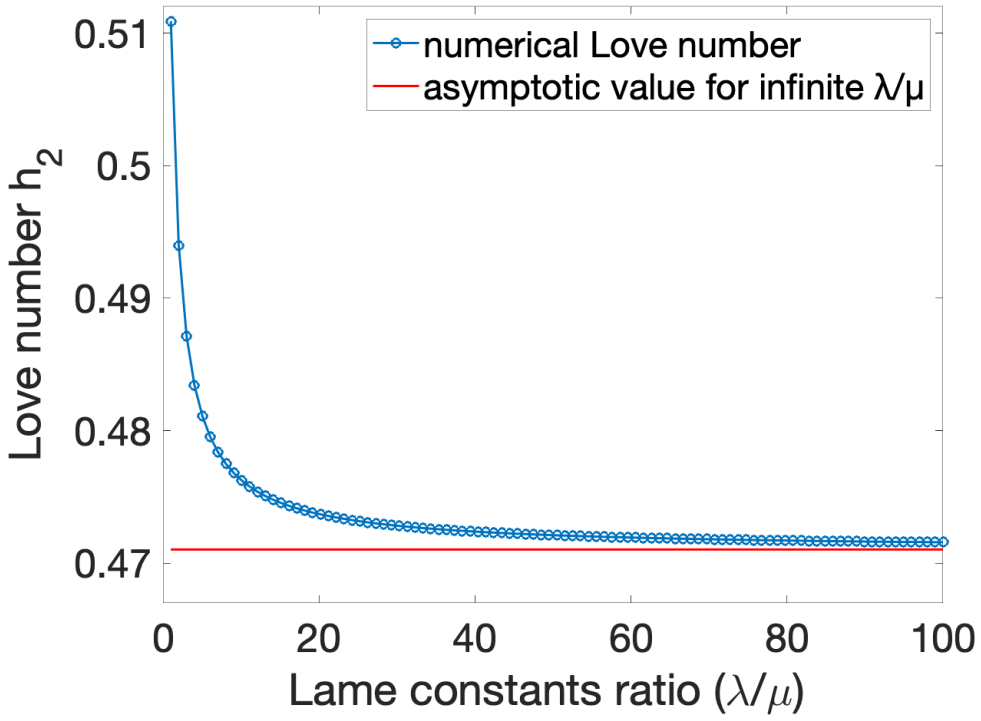

Figure 1 Love numbers of different λ/μ values. The asymptotic value for infinite λ/μ is plotted in red horizontal line, the vertical axis is the Love number h_2.

2.3.2 Non self-gravitation case

We can have an analytical solution for Love number in non self-gravitation planet model. We choose a model with the compressional wave velocity $v_p = 3$ km/s, the shear wave velocity $v_s = 1.2$ km/s and the density $\rho = 2840\ kg/m^3$. The Love number calculated from this model using the analytical solution (2.17) and its definition (2.21). The result $h_2^* = 0.5877$, will be used in the tidal torque calculation in chapter 5. The Mathematica script to get this number can be found in the Appendix.

2.4 Summary

In this chapter, I have introduced the basic theoretical formulation of the tidal force and tidal deformation. I also introduced the Love number that help us understanding tidal deformation without knowing the planet interior. I have compared the influence of the self-gravitation on the tidal deformation.

Chapter 3 Free oscillations of a planet and normal mode frequencies

A planet can resonate as a whole at certain discrete frequencies and spatial patterns. These vibrational modes are called seismic normal modes (p. 337, Aki and Richards, 2002) or free oscillations. We can consider normal modes as the basis functions whose linear combination can represent any seismic wavefield in a planet (Ben-Menahem and Singh, 1981). In this chapter, I will show how to model seismic wavefields in a homogenous solid planet using the normal mode summation.

3.1 Governing equations and boundary conditions

To simplify the problem, we consider a planet as a homogeneous, non-gravitating, elastic sphere. The homogenous equation of motion in the frequency domain can be written as:

$$\alpha^2 \nabla\nabla \cdot \mathbf{u} - \beta^2 \nabla \times \nabla \times \mathbf{u} + \omega^2 \mathbf{u} = \mathbf{0}, \tag{3.1}$$

where $\boldsymbol{u} = \boldsymbol{u_\alpha} + \boldsymbol{u_\beta}$, with $\boldsymbol{u_\alpha}$ being the irrotational part and $\boldsymbol{u_\beta}$ the solenoidal part of the displacement vector, $\nabla \times \boldsymbol{u_\alpha} = 0$, $\nabla \cdot \mathbf{u_\beta} = 0$.

The general solution can be written as (P. 357 eq 6.2, Ben-Menahem and Singh, 2012):

$$\boldsymbol{u}(r,\theta,\phi) = \sum_{l,m} \alpha_{l,m}\ \boldsymbol{M}_{l,m}(r,\theta,\phi) + \beta_{l,m}\boldsymbol{N}_{l,m}(r,\theta,\phi) + \gamma_{l,m}\boldsymbol{L}_{l,m}(r,\theta,\phi)\,, \tag{3.2}$$

where l, m and n are integer numbers. $\alpha_{l,m}$, $\beta_{l,m}$ and $\gamma_{l,m}$ are constants. The M, L, N are known as Hansen vectors, representing different free-oscillation patterns:

$$\begin{aligned} \boldsymbol{L}_{l,m}(r,\theta,\phi) &= \frac{\nabla[j_l(k_\alpha r)Y_l^m(r,\theta)]}{k_\alpha}, \\ \boldsymbol{M}_{\boldsymbol{l,m}}(r,\theta,\phi) &= \nabla \times \left[\boldsymbol{r}\, j_l\left(k_\beta r\right)Y_l^m(r,\theta)\right], \\ \boldsymbol{N}_{l,m}(r,\theta,\phi) &= \nabla \times \frac{\mathbf{M}}{k_\beta}. \end{aligned} \tag{3.3}$$

The superposition of M modes is the SH wave motion of this sphere. Similarly, N indicates SV wave and L indicates P wave motion. These three Hansen vectors are orthogonal to each other in space. $Y_l^m(\theta,\phi)$ is the normalized spherical harmonics. $j_l(k_c r)$ is a spherical Bessel function. $\alpha_{l,m}$, $\beta_{l,m}$ and $\gamma_{l,m}$ are the independent coefficients. The subscript, l, represents the integer angular order which has a range from 0 to positive infinity. The subscript m is also an integer and varying from -l to l. r is the distance from the arbitrary point to the center of the planet. In the spherical coordinates, θ and ϕ are representing an azimuthal location on the sphere which radius is r.

The expansion of the equation (3.3) in terms of spherical unit vector $\boldsymbol{e_r}, \boldsymbol{e_\theta}, \boldsymbol{e_\phi}$ is:

$$\begin{aligned}
\boldsymbol{L}_{l,m}(r,\theta,\phi) &= \frac{\nabla[j_l(k_\alpha r)Y_l^m(r,\theta)]}{k_\alpha} \\
&= \left[\frac{l\, j_l(k_\alpha r)}{k_\alpha r} - j_{l+1}(k_\alpha r)\right] Y_l^m(r,\theta)\boldsymbol{e_r} + \frac{j_l(k_\alpha r)}{k_\alpha r}\frac{\partial Y_l^m(\theta,\phi)}{\partial\theta}\boldsymbol{e_\theta} \\
&\quad + \frac{1}{\sin(\theta)}\frac{j_l(k_\alpha r)}{k_\alpha r}\frac{\partial Y_l^m(\theta,\phi)}{\partial\phi}\boldsymbol{e_\phi}, \\
\boldsymbol{M_{l,m}}(r,\theta,\phi) &= \nabla\times[\boldsymbol{r}\, j_l(k_\alpha r)Y_l^m(r,\theta)] \\
&= -j_l(k_\beta r)\frac{\partial Y_l^m(\theta,\phi)}{\partial\theta}\boldsymbol{e_\phi} + \frac{1}{\sin(\theta)}j_l(k_\beta r)\frac{\partial Y_l^m(\theta,\phi)}{\partial\phi}\boldsymbol{e_\theta}, \\
\boldsymbol{N}_{l,m}(r,\theta,\phi) &= \nabla\times\frac{\mathbf{M}}{k_\beta} = l(l+1)\frac{j_l(k_\beta r)}{k_\beta r}Y_l^m(r,\theta)\boldsymbol{e_r} + \left[(l+1)\frac{j_l(k_\beta r)}{k_\beta r} - \right. \\
&\left. j_{l+1}(k_\beta r)\right]\frac{\partial Y_l^m(\theta,\phi)}{\partial\theta}\boldsymbol{e_\theta} + \left[(l+1)\frac{j_l(k_\beta r)}{k_\beta r} - j_{l+1}(k_\beta r)\right]\frac{1}{sin(\theta)}\frac{\partial Y_l^m(\theta,\phi)}{\partial\phi}\boldsymbol{e_\phi},
\end{aligned} \tag{3.4}$$

where $k_\beta = \omega/v_\beta$, $k_\alpha = \omega/v_\alpha$. v_α is the propagation velocity of the P wave. v_β is the velocity of the S wave. Therefore, we can rewrite the **M, L, N** as following by using surface normalized spherical harmonic vectors **R, S, T** from equation (2.10):

$$\boldsymbol{L}_{l,m}(r,\theta,\phi) = \left[\frac{l\, j_l(k_\alpha r)}{k_\alpha r} - j_{l+1}(k_\alpha r)\right]\boldsymbol{R_l^m}(\theta,\phi) + \sqrt{l(l+1)}\frac{j_l(k_\alpha r)}{k_\alpha r}\boldsymbol{S_l^m}(\theta,\phi), \tag{3.5}$$

$$\boldsymbol{M_{l,m}}(r,\theta,\phi) = \sqrt{l(l+1)}j_l(k_\beta r)\boldsymbol{T}_l^m(\theta,\phi),$$

$$\boldsymbol{N}_{l,m}(r,\theta,\phi) = l(l+1)\frac{j_l(k_\beta r)}{k_\beta r}\boldsymbol{R}_l^{\boldsymbol{m}}(\theta,\phi) + \sqrt{l(l+1)}\left[(l+1)\frac{j_l(k_\beta r)}{k_\beta r} - j_{l+1}(k_\beta r)\right]\boldsymbol{S}_l^{\boldsymbol{m}}(\theta,\phi).$$

By substituting equation (3.5) into (3.2) and compare the coefficients of spherical harmonic vectors **R, S, T**, we can express the radial function $U(r)$, $V(r)$ and $W(r)$ using undetermined coefficients $\alpha_{l,m}$, $\beta_{l,m}$ and $\gamma_{l,m}$:

$$U(r) = \gamma_{l,m}\left[\frac{l\, j_l(k_\alpha r)}{k_\alpha r} - j_{l+1}(k_\alpha r)\right] + \beta_{l,m}\left[l(l+1)\frac{j_l(k_\beta r)}{k_\beta r}\right],$$

$$V(r) = \sqrt{l(l+1)}\left\{\gamma_{l,m}\left[\frac{j_l(k_\alpha r)}{k_\alpha r}\right] + \beta_{l,m}\left[l(l+1)\frac{j_l(k_\beta r)}{k_\beta r} - j_{l+1}(k_\beta r)\right]\right\}, \tag{3.6}$$

$$W(r) = \sqrt{l(l+1)}\alpha_{l,m}\, j_l(k_\beta r).$$

Here, we have successfully separated the radial part and azimuthal part of normal modes. The rest of the work is only to determine the coefficients, $\alpha_{l,m}$, $\beta_{l,m}$ and $\gamma_{l,m}$, using the boundary conditions (zero surface traction).

We assume the planet has a perfect free surface condition, which is traction $\boldsymbol{T_r}$ is zero in all three components. In a homogeneous elastic medium, we apply the constitutive relation which only have two independent constants to get the surface traction:

$$\boldsymbol{T_r} = \sigma \cdot \mathbf{e_r} = \lambda \nabla \cdot \mathbf{u}\, \mathbb{I} \cdot \mathbf{e_r} + \mu(\nabla \mathbf{u} + \mathbf{u}\nabla) \cdot \mathbf{e_r}, \tag{3.7}$$

where σ is the traction tensor. $\mathbb{I}$ is an identity matrix. $\mathbf{e_r}$ is the unit vector along the radial direction. λ and μ are Lamé constants.

By substituting equation (3.6) into (3.7), we can get

$$\boldsymbol{T_r}(r,\theta,\phi) = \left[\lambda\left(\frac{2\,U(r)}{r} - l(l+1)\frac{V(r)}{r} + \frac{dU(r)}{dr}\right) + \mu\frac{dU(r)}{dr}\right]\boldsymbol{R_l^m}(\theta,\phi) + \sqrt{l(l+1)}\left[\frac{U(r)-V(r)}{r} + \frac{dV(r)}{dr}\right]\boldsymbol{S_l^m}(\theta,\phi) + \sqrt{l(l+1)}\left[\frac{dW(r)}{dr} - \frac{W(r)}{r}\right]\boldsymbol{T_l^m}(\theta,\phi). \tag{3.8}$$

By letting the surface traction inequation (3.8) to zero, we can get three equations:

$$\beta_{l,m}\frac{2\mu l(l+1)\left[(l-1)j_l(k_\beta r) - k_\beta\, r\, j_{l+1}(k_\beta r)\right]}{k_\beta r^2} + \gamma_{l,m}\frac{[2l(l-1)\mu - (k_\alpha r)^2(\lambda+2\mu)]j_l(k_\alpha r) + 4\mu k_\alpha r j_{l+1}(k_\alpha r)}{k_\alpha r^2} = 0, \tag{3.9}$$

$$\beta_{l,m}\frac{\mu\left[\left(-2+2l^2-(k_\beta r)^2\right)j_l(k_\beta r)+2k_\beta\, r\, j_{l+1}(k_\beta r)\right]}{k_\beta r^2} - \gamma_{l,m}\frac{2\mu[(1-l)j_l(k_\alpha r)+k_\alpha r j_{l+1}(k_\alpha r)]}{k_\alpha r^2} = 0, \tag{3.10}$$

$$\alpha_{l,m}\,\mu\frac{(l-1)j_l(k_\beta r) - k_\beta\, r\, j_{l+1}(k_\beta r)}{k_\beta r^2} = 0 \tag{3.11}$$

In the above equations we can replace the μ and λ by v_α and v_β by the following relation:

$$\mu = \rho {v_\beta}^2, \qquad \lambda = \rho\left({v_\alpha}^2 - 2{v_\beta}^2\right). \tag{3.12}$$

In equation (3.9), (3.10) and (3.11), the coefficients $\alpha_{l,m}$, $\beta_{l,m}$, $\gamma_{l,m}$ are non-trivial only for a particular set of discrete eigenfrequencies, ω's, embedded in $k_\beta$and k_α. These frequencies are called normal mode frequencies, which will be solved in the next section.

3.2 Eigen-frequencies and normal modes

3.2.1 Toroidal modes

There are two kinds of normal modes, one is called spheroidal modes, the other is called toroidal modes. They have two different sets of frequencies. We can use equation (3.9) and (3.10) to solve the frequencies for the spheroidal modes, and use (3.11) to solve for the toroidal frequencies. First, to solve eigen-frequencies of toroidal modes, we transform equation (3.11) into:

$$(l-1)j_l\left(\frac{\omega}{v_\beta}a\right)-\frac{\omega}{v_\beta}\,a\,j_{l+1}\left(\frac{\omega}{v_\beta}a\right)=0, \tag{3.13}$$

where a is the radius of the planet, j_l is the spherical Bessel function of the angular order l ($l = 0,1,2 \ldots$), k_α and k_β are the P and S wavenumbers respectively, and $\tau = k_\beta/k_\alpha$. The temporary frequencies are included in wavenumbers as, $k_\alpha = \frac{\omega}{v_p}, k_\beta = \frac{\omega}{v_s}$. As an example, we can solve equation (3.13) to get the frequencies of toroidal modes (Figure 2).

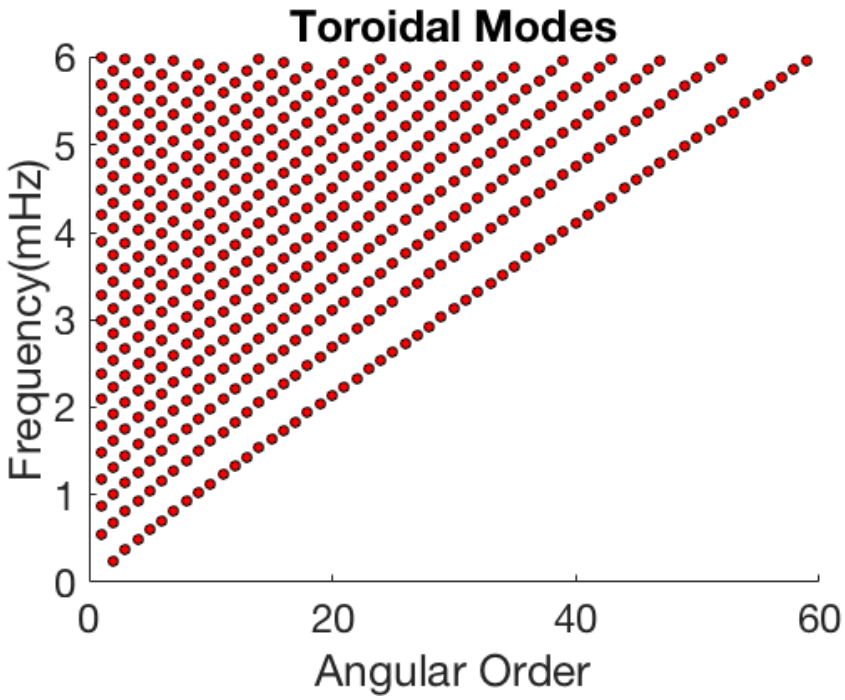

Figure 2 The toroidal modes frequencies at different angular orders. The planet has 2000km in radius, the compressional wave velocity of the planet is $v_p = 3$ km/s, the shear wave velocity $v_s = 1.2$ km/s and the density of the planet is 2840 kg/m^3.

3.2.2 Spheroidal modes

The second kind of oscillations is known as spheroidal mode. To find the eigen-frequencies for the spheroidal modes, we let equation (3.9) and (3.10) be zero and eliminate $\beta_{l,m}$ and $\gamma_{l,m}$:

$$\frac{2\ (1 - l + k_\alpha a\, S_a)}{\left[-2 + 2l^2 - \left(k_\beta a\right)^2 + 2k_\beta\, aS_b\right]} - \frac{[2l(l-1) - (k_\alpha a)^2\tau^2 + 4k_\alpha a S_a]}{2l(l+1)\left[(l-1) - k_\beta\, a\, S_b\right]} = 0, \qquad (3.14)$$

where a is the planet radius, $S_\alpha = j_{l+1}(k_\alpha a)/j_l(k_\alpha a)$, $S_\beta = j_{l+1}(k_\beta a)/j_l(k_\beta a)$, j_l is the spherical Bessel function of the angular order l (l=0,1,2...), k_α and k_β are the P and S wavenumbers respectively, and $\tau = k_\beta/k_\alpha$. The temporary frequencies are included in wavenumbers as, $k_\alpha = \frac{\omega}{v_p}, k_\beta = \frac{\omega}{v_s}$. For example, we can solve equation (3.14) to get the frequencies of spheroidal modes (Figure 3).

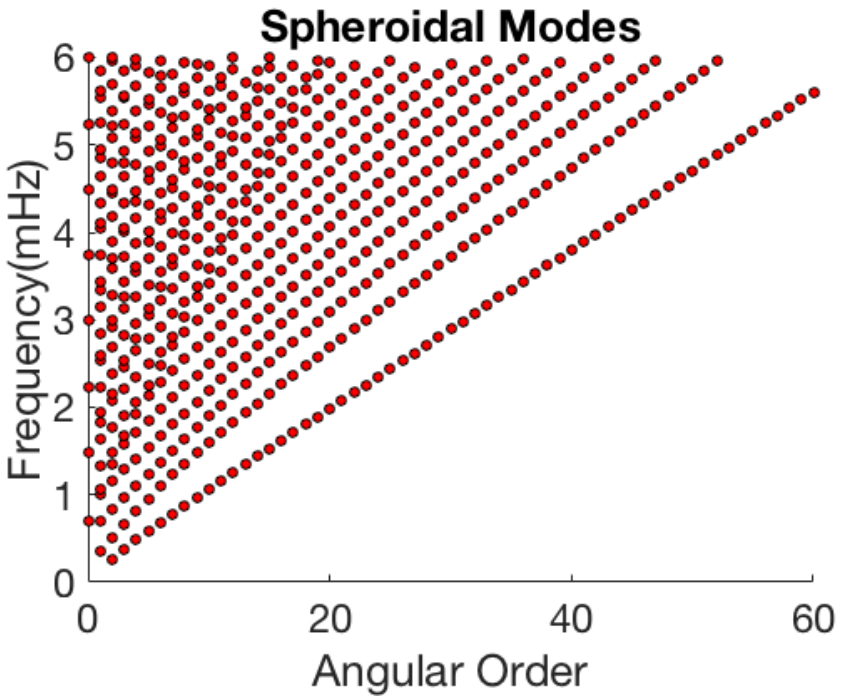

Figure 3 The spheroidal modes frequencies at different angular orders. The planet has 2000km in radius, the compressional wave velocity of the planet is $v_p = 3$ km/s, the shear wave velocity $v_s = 1.2$ km/s and the density of the planet is 2840 kg/m^3.

3.3 Normalization of normal modes

We used three constants $\alpha_{l,m}, \beta_{l,m}, \gamma_{l,m}$ to represent the excitation coefficients of the modes. To make the modes "unit vectors", we need to normalize the normal modes. We need to make sure the inner product of the same modes is 1 and the inner product of different modes is 0:

$$\langle \rho \boldsymbol{u_i}, \boldsymbol{u_j} \rangle = \delta_{ij}, \tag{3.15}$$

where $\delta_{ij} = 1$ if $i = j$, $\delta_{ij} = 0$, if $i \neq j$.

We can first normalize the spheroidal modes. As we defined before in equation (2.10) and (2.11), we calculate the inner product as a volume integral in the space domain of the planet:

$$\iiint \rho\big[\,{}_nU_l(r)\boldsymbol{R}_l^{\boldsymbol{m}}(\theta,\phi) + \;{}_nV_l(r)\boldsymbol{S}_l^{\boldsymbol{m}}(\theta,\phi)\big]\big[{}_{n'}U_{l'}(r)\boldsymbol{R}_{l'}^{\boldsymbol{m'}}(\theta,\phi) + {}_{n'}V_{l'}(r)\boldsymbol{S}_{l'}^{\boldsymbol{m'}}(\theta,\phi)\big]^{*} r^2\sin(\theta)\,dr d\theta d\phi. \tag{3.16}$$

Because of the orthogonality of spherical harmonic vectors **R, S**:

$$\begin{aligned}
\iint \boldsymbol{R}_l^{\boldsymbol{m}}(\theta,\phi)\boldsymbol{R}_{l'}^{-\boldsymbol{m'}}(\theta,\phi)\sin(\theta)\,d\theta d\phi &= \delta_{mm'}\delta_{ll'},\\
\iint \boldsymbol{S}_l^{\boldsymbol{m}}(\theta,\phi)\boldsymbol{S}_{l'}^{-\boldsymbol{m'}}(\theta,\phi)\sin(\theta)\,d\theta d\phi &= \delta_{mm'}\delta_{ll'},\\
\iint \boldsymbol{R}_l^{\boldsymbol{m}}(\theta,\phi)\boldsymbol{S}_{l'}^{-\boldsymbol{m'}}(\theta,\phi)\sin(\theta)\,d\theta d\phi &= 0,\\
\iint \boldsymbol{S}_l^{\boldsymbol{m}}(\theta,\phi)\boldsymbol{R}_{l'}^{-\boldsymbol{m'}}(\theta,\phi)\sin(\theta)\,d\theta d\phi &= 0.
\end{aligned} \tag{3.17}$$

The equation (3.16) can be simplified to:

$$\int_0^a \big[\,{}_nU_l(r)\,{}_{n'}U_{l'}(r) + \;{}_nV_l(r)\,{}_{n'}V(r)\big]\rho r^2 dr\delta_{mm'}\delta_{ll'}, \tag{3.18}$$

where a is the radius of the planet. If $n \neq n'$ or $l \neq l'$ the term will be automatically vanished, (3.18) can be further reduced to

$$\int_0^a \big[\,{}_nU_l^2(r) + \;{}_nV_l^2(r)\big]\rho r^2 dr = 1. \tag{3.19}$$

Here we use equation (3.14) to first solve eigen-frequencies $\omega_{l,n}$ where n (the number of zero crossings along the radial direction) indicates the index of the eigen-frequencies ranging from 0 to positive infinity. Next, we can determine the ratio $\epsilon_{l,n} = \frac{\beta_{l,m,n}}{\gamma_{l,m,n}}$ by using (3.9) or (3.10):

$$\begin{aligned}
\epsilon_{l,n} = \frac{\beta_{l,m,n}}{\gamma_{l,m,n}} &= \frac{2\,k_\beta\,(1-l+k_\alpha r\,S_a)j_l(k_\alpha r)}{k_\alpha\left[-2+2l^2-\left(k_\beta r\right)^2+2k_\beta\,rS_b\right]j_l\left(k_\beta r\right)},\\
\epsilon_{l,n} = \frac{\beta_{l,m,n}}{\gamma_{l,m,n}} &= \frac{k_\beta[2l(l-1)-(k_\alpha r)^2\tau^2+4k_\alpha rS_a]j_l(k_\alpha r)}{2k_\alpha l(l+1)\big[(l-1)-k_\beta\,r\,S_b\big]j_l\left(k_\beta r\right)}.
\end{aligned} \tag{3.20}$$

Now, we can replace β with $\gamma\epsilon$ in equation (3.6):

$$
\begin{aligned}
{}_nU_l(r) &= \gamma_{l,m,n}\left[\frac{l\, j_l(k_\alpha r)}{k_\alpha r} - j_{l+1}(k_\alpha r)\right] + \beta_{l,m,n}\epsilon_{l,n}\left[l(l+1)\frac{j_l(k_\beta r)}{k_\beta r}\right], \\
{}_nV_l(r) &= \sqrt{l(l+1)}\left\{\gamma_{l,m,n}\left[\frac{j_l(k_\alpha r)}{k_\alpha r}\right] + \beta_{l,m,n}\epsilon_{l,n}\left[l(l+1)\frac{j_l(k_\beta r)}{k_\beta r} - j_{l+1}(k_\beta r)\right]\right\}.
\end{aligned}
\tag{3.21}
$$

By substituting equation (3.21) into equation (3.19), we can solve for $\gamma_{l,m}$ for every l and m:

$$
\begin{aligned}
\gamma_{l,m,n} = 1/\int_0^a \Bigg[&\left[\frac{l\, j_l(k_\alpha r)}{k_\alpha r} - j_{l+1}(k_\alpha r)\right] + \epsilon_{l,n}\left[l(l+1)\frac{j_l(k_\beta r)}{k_\beta r}\right]^2 + l(l+ \\
&1)\left\{\left[\frac{j_l(k_\alpha r)}{k_\alpha r}\right] + \epsilon_{l,n}\left[l(l+1)\frac{j_l(k_\beta r)}{k_\beta r} - j_{l+1}(k_\beta r)\right]\right\}^2 .\Bigg] \rho r^2 dr.
\end{aligned}
\tag{3.22}
$$

$\beta_{l,m,n}$ can be simply calculated by $\beta_{l,m,n} = \epsilon_{l,n}\gamma_{l,m,n}$.

Similarly, we can normalize the toroidal modes from equation (3.15):

$$
\langle \rho \boldsymbol{u_i}, \boldsymbol{u_j} \rangle = 1 = \iiint \rho\left[{}_nW_l(r)\boldsymbol{T}_l^m(\theta,\phi)\right]\left[{}_{n'}W_{l'}(r)\boldsymbol{T}_{l'}^{m'}(\theta,\phi)\right]^* r^2 \sin(\theta)\, dr d\theta d\phi.
\tag{3.23}
$$

Because the orthogonality of spherical harmonic vectors **T:**

$$
\iint \boldsymbol{T}_l^{\boldsymbol{m}}(\theta,\phi)\boldsymbol{T}_{l'}^{-\boldsymbol{m'}}(\theta,\phi)\sin(\theta)\, d\theta d\phi = \delta_{mm'}\delta_{ll'},
\tag{3.24}
$$

equation (3.23) can be simplified as:

$$
\int_0^a {}_nW_l^2(r)\, r^2 dr = 1.
\tag{3.25}
$$

In short, we use equation (3.13) to solve for the toroidal eigen-frequencies and we solve for the coefficients $\alpha_{l,m}$ in equation (3.6) as:

$$\alpha_{l,m,n} = 1/\int_0^a \left[\sqrt{l(l+1)}\, j_l(k_\beta r)\right]^2 r^2 dr. \tag{3.26}$$

In conclusion, the fully normalized normal modes of a homogenous spherical planet can be written as:

spheroidal:

$$ {}_n\boldsymbol{u}_l^m(r,\theta,\phi,\omega_{l,n}) = {}_nU_l(r)\boldsymbol{R}_l^{\boldsymbol{m}}(\theta,\phi) + \sqrt{l(l+1)}\ {}_nV_l(r)\boldsymbol{S}_l^{\boldsymbol{m}}(\theta,\phi), \tag{3.27}$$

toroidal:

$$ {}_n\boldsymbol{u}_l^m(r,\theta,\phi,\omega_{l,n}) = \sqrt{l(l+1)}\ {}_nW_l(r)\boldsymbol{T}_l^m(\theta,\phi), \tag{3.28}$$

where ${}_nU_l(r)$, ${}_nV_l(r)$ and ${}_nW_l(r)$ are containing the fully normalized coefficients $\alpha_{l,m,n}$, $\beta_{l,m,n}$ and $\gamma_{l,m,n}$.

3.4 Normal mode summation for making synthetic seismograms

The linear superposition of normal modes could form any dynamic motion interior of an elastic sphere. In this section of the dissertation, I will demonstrate how to synthesize seismogram using summation of the normal modes.

With a force acting on a unit space in the homogeneous planet, the equation of motion in the time domain is:

$$-(\lambda+2\mu)\nabla\nabla\cdot\mathbf{u} + \mu\nabla\times\nabla\times\mathbf{u} + \rho\frac{\mathrm{d}^2\mathbf{u}}{\mathrm{dt}^2} = \mathbf{F}(\mathrm{t}). \tag{3.29}$$

In the frequency domain, it becomes:

$$-(\lambda+2\mu)\nabla\nabla\cdot\mathbf{u} + \mu\nabla\times\nabla\times\mathbf{u} - \rho\omega^2\mathbf{u} = \mathbf{F}(\omega), \tag{3.30}$$

where $\mathbf{F}(\omega)$ is the force in Newton per unit volume in the frequency domain. For simplification we write the displacement field of the placement in the frequency domain using the summation of the normal modes as:

$$\mathbf{u} = \sum_{i} a_i \boldsymbol{u_i}, \tag{3.31}$$

where a_i is the coefficient of the i-th mode $\boldsymbol{u_i}$. This expression is equivalent to equation (3.2). We define an operator $\boldsymbol{L}$:

$$\boldsymbol{L}(\boldsymbol{u_i}) = -(\lambda + 2\mu)\nabla\nabla \cdot \boldsymbol{u_i} + \mu\nabla \times \nabla \times \boldsymbol{u_i}, \tag{3.32}$$

we can get:

$$\sum_{i} a_i(\boldsymbol{L}(\boldsymbol{u_i}) - \rho\omega_i^2 \mathbf{u_i}) = \mathbf{F}(\omega_i). \tag{3.33}$$

However, using the operator $\boldsymbol{L}$**,** we can write the equation of motion (3.1) as:

$$\boldsymbol{L}(\boldsymbol{u_i}) - \rho\omega_i^2 \mathbf{u_i} = \mathbf{0}. \tag{3.34}$$

The solution of this equation is the normal mode we obtained earlier and should be normalized by:

$$\langle \rho \boldsymbol{u_i}, \boldsymbol{u_j} \rangle = \delta_{ij}. \tag{3.35}$$

We can multiply $\boldsymbol{u_j}$ on both sides of the equation (3.34) and transform it to:

$$\langle \boldsymbol{L}\boldsymbol{u_i}, \boldsymbol{u_j} \rangle - \omega_i^2 \delta_{ij} = 0. \tag{3.36}$$

The seismic displacement wavefield of the planet in time domain can be written as:

$$\boldsymbol{u}(t) = \sum_{i} a_i \, \mathbf{u_i} \, e^{-i\,\omega_i\, t}, \tag{3.37}$$

where t is the time. Its Laplace transformed form is:

$$\boldsymbol{u}(s) = \sum_{i} a_i \frac{\mathbf{u_i}}{s + i\omega}. \tag{3.38}$$

To determine the coefficient a_i, we insert (3.38) into (3.29) and get the equation of motion in the Laplacian domain:

$$\rho\, s^2 \sum_{\boldsymbol{i}} a_i \frac{\mathbf{u_i}}{s+i\omega} + \sum_{\boldsymbol{i}} a_i \frac{\boldsymbol{L(u_i)}}{s+i\omega} = \mathbf{F}(s), \tag{3.39}$$

where $\mathbf{F}(s)$ is $\mathbf{F}(t)$ in the Laplacian domain. If we let $\mathbf{u_j}$ do an inner product with (3.39), we can get the following equation using the relation (3.36):

$$s^2 \sum_{\boldsymbol{i}} a_i \frac{\delta_{ij}}{s+i\omega} + \sum_{\boldsymbol{i}} \frac{\omega_i^2 \delta_{ij}}{s+i\omega} = \langle \mathbf{F}(s), \boldsymbol{u_j} \rangle. \tag{3.40}$$

We can get the expression of a_j:

$$a_j = \frac{(s+i\,\omega)}{s^2+\omega_j^2} \langle \mathbf{F}(s), \boldsymbol{u_j} \rangle. \tag{3.41}$$

We insert (3.41) into (3.38),we can get:

$$\boldsymbol{u}(s) = \sum_{\boldsymbol{i}} a_i \frac{\mathbf{u_i}}{s+i\omega} = \sum_{\boldsymbol{i}} \frac{\langle \mathbf{F}(s), \boldsymbol{u_i} \rangle \mathbf{u_i}}{(s^2+\omega_i^2)}. \tag{3.42}$$

If the source time force is a delta function:

$$\begin{aligned} \delta(t) &= 0 \; if \; t \neq 0; \\ \delta(t) &= 1 \; if \; t = 0. \end{aligned} \tag{3.43}$$

We write the single force at location $\boldsymbol{r_s}$ as:

$$\mathbf{F}(t) = \boldsymbol{F}\delta(t)\delta(\boldsymbol{r}-\boldsymbol{r_s}), \tag{3.44}$$

where $\boldsymbol{F}$ is a single force vector. Its Laplacian transformation is $\mathbf{F}(s) = F\delta(\boldsymbol{r}-\boldsymbol{r_s})$. If we insert it to (3.42), we can get:

$$\boldsymbol{u}(s,\boldsymbol{r}) = \sum_{\boldsymbol{i}} \frac{(\boldsymbol{F}\cdot \mathbf{u}(\boldsymbol{r_s})_{\mathbf{i}}^{*})\mathbf{u}(\mathbf{r})_{\mathbf{i}}}{(s^2+\omega_i^2)}, \tag{3.45}$$

We can transform (3.45) back to time domain:

$$\boldsymbol{u}(t,\boldsymbol{r}) = \sum_{\boldsymbol{i}} (\boldsymbol{F}\cdot\mathbf{u}(\boldsymbol{r_s})^{*}_{\mathbf{i}})\mathbf{u}(\mathbf{r})_{\mathbf{i}}\sin(\omega_i t). \tag{3.46}$$

The attenuation effect can be included by adding Q factor as:

$$\boldsymbol{u}(t,\boldsymbol{r}) = \sum_{\boldsymbol{i}} (\boldsymbol{F}\cdot\mathbf{u}(\boldsymbol{r_s})^{*}_{\mathbf{i}})\mathbf{u}(\mathbf{r})_{\mathbf{i}}\mathrm{e}^{-\frac{\omega_i}{2Q}\mathrm{t}}\sin(\omega_i\, t). \tag{3.47}$$

For a moment tensor source $\boldsymbol{M}$, we can get the solution of seismic displacement field as:

$$\begin{gathered}\boldsymbol{u}(t,\boldsymbol{r}) = \sum_{\boldsymbol{i}} (\boldsymbol{M}\colon\mathbf{e}(\boldsymbol{r_s})^{*}_{\mathbf{i}})\mathbf{u}(\mathbf{r})_{\mathbf{i}}\mathrm{e}^{-\frac{\omega_i}{2Q}\mathrm{t}}\sin(\omega_i\, t),\\ \boldsymbol{e} = \frac{\boldsymbol{\nabla u} + \boldsymbol{u\nabla}}{2},\end{gathered} \tag{3.48}$$

where $\boldsymbol{e}$ is the strain tensor.

3.5 Summary

From first principles, I derived the spheroidal and toroidal modes along with their frequencies for a homogenous planet. The modes frequencies will be compared with the tidal force frequencies in Chapter 2 to determine whether resonance can occur. I also showed how to use normal mode summation to generate synthetic seismogram for a single force source and a moment tensor source. I will use this analytical solution to benchmark the proposed boundary element method in Chapter 4.

Chapter 4 Boundary element method for irregular bodies seismic modeling

I will introduce a 3-D elastic Boundary Element Method (BEM) computer code, called AstroSeis. I will show its ability to model seismic wavefields in a body with an arbitrary shape, such as an asteroid, or a planet with very complex topography. I will benchmark AstroSeis against other existing methods such as normal mode summation (Chapter 3) and the direct solution method (DSM)(Kawai *et al.*, 2006). This open-source AstroSeis will be a useful tool to study the interior and surface processes of asteroids and planets.

4.1 Method and boundary integral equations

4.1.1 A solid asteroid with topography

First, I will show how to use BEM to model seismic wavefield in a solid asteroid. We assume the asteroid is a homogenous solid body with an irregular boundary. In BEM, we only need to know the wavefield on the boundary and we can then compute the wavefield in the entire model.

The boundary integral equation governs the surface seismic displacement field, **u** for an interior domain Ω (Figure 4a), reads,

$$\chi(\mathbf{x})\mathrm{u_n}(\mathbf{x}) = \mathrm{u_{0_n}}(\mathbf{x}) + \iint_{\mathrm{S}} \left[\mathrm{G_{ni}}(\mathbf{x}', \mathbf{x}, \omega) t_{\mathrm{i}}(\mathbf{x}') - \mathrm{u_i}(\mathbf{x}')\mathrm{C_{ijkl}}(\mathbf{x}')\mathrm{G_{nk,l}}(\mathbf{x}', \mathbf{x}, \omega)\mathrm{n_j}\right]\mathrm{d}\mathbf{x}'^{\mathbf{2}}. \tag{4.1}$$

In this equation, S is the surface of the elastic body including topography. $\chi(\boldsymbol{x}) = 1$ if $\boldsymbol{x} \in \Omega$ and $\chi(\boldsymbol{x}) = \frac{\mathbf{1}}{\mathbf{2}}$ if $\boldsymbol{x} \in$ S. The surface integral should be understood in the sense of the Cauchy principal value if $\boldsymbol{x}$ is on the boundary. In BEM, $\boldsymbol{x}'$ and $\boldsymbol{x}$ are points on S; n_j is the outward surface normal at $\boldsymbol{x}'$; $C_{ijkl}(\boldsymbol{x}')$ is the elastic tensor at $\boldsymbol{x}'$. Here, we assume the

medium is isotropic and that there are only two independent Lamé parameters in C_{ijkl}. $G_{nk}(\boldsymbol{x}', \boldsymbol{x}, \omega)$ is the Green's function, the displacement wavefield along the k-th direction recorded at $\boldsymbol{x}'$ caused by a single-force source at $\boldsymbol{x}$ with the force direction along the n-th direction. $G_{kn,l}(\boldsymbol{x}', \boldsymbol{x}, \omega)$ is the spatial directional derivative of the elastic Green's function with respect to $\boldsymbol{x}'$ along the l-th direction in the frequency domain. All subscripts (n, i, j, k, l) in equation (4.1).take a value of 1, 2, or 3 to indicate the component of the vector/tensor field. Because the surface traction, $t_i(\boldsymbol{x}')$, is zero on the free surface, we can neglect it in equation (4.1).

In equation (4.1), $u_{0_{\boldsymbol{n}}}$ is the incident field. For a single-force source $\boldsymbol{f}$, we can directly use Green's function to calculate the incident field:

$$\mathrm{u}_{0_{\mathbf{n}}}(\mathbf{x}) = \iiint_{\boldsymbol{\Omega}} \mathrm{f_i}(\mathbf{x}')\delta(\mathbf{x}' - \mathbf{x_0})\mathrm{G_{ni}}(\mathbf{x}, \mathbf{x}', \omega)\mathrm{d}\mathbf{x}'^3, \tag{4.2}$$

where Ω is the space enclosed by surface S, $\boldsymbol{x}$ is a point on surface S, $\boldsymbol{x}'$ is a point in Ω. $f_i(\boldsymbol{x}')$ is the single force at $\boldsymbol{x}'$along the i-th direction. $\boldsymbol{x_0}$ is the location of the source within Ω (Figure 4a).

If the source is a 3-by-3 moment tensor, M_{ij}, the incident field is calculated as follows:

$$\mathrm{u}_{0_{\mathbf{n}}}(\mathbf{x}) = \iiint_{\Omega} \mathrm{M_{ij}}\delta(\mathbf{x}' - \mathbf{x_0})\mathrm{G_{ni,j}}(\mathbf{x}, \mathbf{x}', \omega)\mathrm{d}\mathbf{x}'^3. \tag{4.3}$$

We can solve equation (4.1) for $\boldsymbol{u}(\boldsymbol{x})$ on the boundary, $\boldsymbol{x} \in S$. We partition the surface into small triangles. Each triangle is called a boundary element. The I-th element is called Σ_I (Figure 4a). We assume the seismic wavefield $\boldsymbol{u}(\boldsymbol{x})$ on each surface element is constant. We can then discretize equation (4.1) and get a system of linear equations:

$$\left(\frac{1}{2}\mathbb{I} + \mathrm{T}\right)[\mathrm{u}] = [\mathrm{u_0}], \tag{4.4}$$

$[u]$ is a column vector containing the 3-component surface displacements (i.e., the total field including the incident field and scattered fields) on all the elements. $\mathbb{I}$ is an identity matrix.

$[u_0]$ is a column vector containing the incident field on all surface elements excited by a single-force or a moment tensor source calculated using equation (4.2) or (4.3).

We define a matrix representing the pair-wise field interaction between elements:

$$\mathrm{T}(I, I') = \iint_{\Sigma_{I'}} (\mathbf{x}')\mathrm{C}_{\mathrm{ijkl}}(\mathbf{x}')\mathrm{G}_{\mathrm{nk,l}}(\mathbf{x}', \mathbf{x_I}, \omega)\mathrm{n_j}\mathrm{d}\mathbf{x'^2}. \quad (4.5)$$

where I and I' are boundary element indices on S. They are also representing row index and column index of T matrix.

In the BEM method, we first obtain the surface displacement $[u]$ on each element by solving the linear algebraic equation (4.4). The wavefield at any interior point can be calculated using equation (4.1) using $\chi(\boldsymbol{x}) = 1$ for any interior point $\boldsymbol{x}$ in Ω.

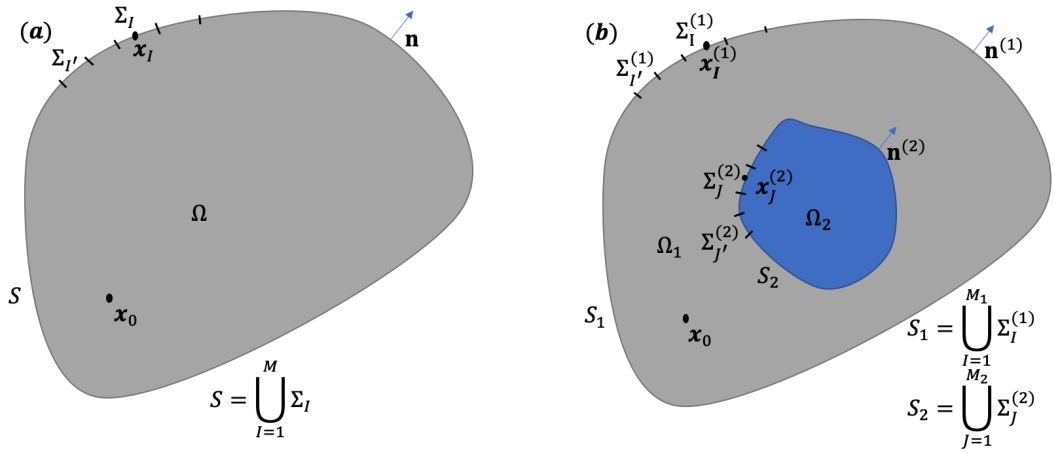

Figure 4 Geometry used in BEM. (a) A solid asteroid. The domain in gray is the solid medium Ω. S is the surface of this domain. We partition the surface into M small triangles. Σ_I and $\Sigma_{I'}$ are boundary elements on S with indices I and I', respectively. x_I is the collocation point on the element Σ_I which is defined as the center of the inscribed circle on Σ_I. x_0 is the location of the source. n is the surface normal on S. (b) A solid body with a liquid core schematic. Ω_1 is representing the solid medium which is the space in gray. Ω_2 is representing the liquid medium which is the space in blue. J and J' are element indices on S_2.

4.1.2 Solid body with a liquid core

In this section, we show the BEM modeling for a solid body with a liquid core (Figure 4b). Because of the liquid core in the solid body, we now have two boundaries. We refer to the outer free surface as S_1, and the interface between liquid and solid as S_2. Because we divide the surfaces into discrete triangles or boundary elements, we define the I-th and I'-th boundary element on S_1 as $\Sigma_I^{(1)}$ and $\Sigma_{I'}^{(1)}$, respectively. We also define the J-th and J'-th boundary element on S_2 as $\Sigma_J^{(2)}$ and $\Sigma_{J'}^{(2)}$ (Figure 4b), respectively.

For a seismic wavefield in a liquid medium, the Green's function is simply $G_P = e^{ik_\alpha r}/(4\pi r)$, where $k_\alpha = \omega/v_p$ is the wavenumber in the liquid, ω the angular frequency,

and r the source-receiver distance. We have the boundary integral equation in the liquid medium:

$$\chi(\mathbf{x})\mathrm{P}(\mathbf{x}) = \mathrm{P}_0(\mathbf{x}) - \iint_{\mathrm{S}_2} [\frac{\partial \mathrm{G_P}(\mathbf{x}',\mathbf{x})}{\partial \mathbf{n}^{(2)}(\mathbf{x}')} \mathrm{P}(\mathbf{x}') - \mathrm{G_P}(\mathbf{x}',\mathbf{x}) \frac{\partial \mathrm{P}(\mathbf{x}')}{\partial \mathbf{n}^{(2)}(\mathbf{x}')}] \mathrm{d}\mathbf{x}'^{\mathbf{2}}, \tag{4.6}$$

where $\chi(\boldsymbol{x}) = 1$ if $\boldsymbol{x} \in \Omega_2$ and $\chi(\boldsymbol{x}) = \frac{\mathbf{1}}{\mathbf{2}}$ if $\boldsymbol{x} \in S_2$. P is the total pressure field and P_0 is the incident pressure field on the fluid boundary, S_2. $\boldsymbol{x}'$ is a point on S_2. $\boldsymbol{x}$ can be either on S_2 or inside the domain Ω_2. $\mathbf{n}^{(2)}(\boldsymbol{x}')$ is the outward surface normal at $\boldsymbol{x}'$. We can discretize equation (4.6) using the following matrices (see Figure 4b for the meaning of the symbols):

$$\begin{aligned} A(J,J') &= \iint_{\Sigma_{J'}^{(2)}} \frac{\partial \mathrm{G_P}(\mathbf{x}',\mathbf{x}_J)}{\partial \mathbf{n}^{(2)}(\mathbf{x}')} \mathrm{d}\mathbf{x}'^{\mathbf{2}}, \mathbf{x}' \in \Sigma_{J'}^{(2)}, \\ B(J,J') &= \iint_{\Sigma_{J'}^{(2)}} \mathrm{G_P}(\mathbf{x}',\mathbf{x}_J)\, \mathrm{d}\mathbf{x}'^{\mathbf{2}}, \mathbf{x}' \in \Sigma_{J'}^{(2)}. \end{aligned} \tag{4.7}$$

In the solid domain, we write the BIE as

$$\begin{aligned} \chi(\boldsymbol{x})u_n(\boldsymbol{x}) = {} & u_{0_{\boldsymbol{n}}}(\boldsymbol{x}) \\ & + \iint_{S_1 \cup S_2} \big[G_{ni}(\boldsymbol{x}',\boldsymbol{x},\omega)T_i(\boldsymbol{x}') \\ & - u_i(\boldsymbol{x}')C_{ijkl}(\boldsymbol{x}')G_{nk,l}(\boldsymbol{x}',\boldsymbol{x},\omega)n_j(\boldsymbol{x}')\big] d\boldsymbol{x}'^{\mathbf{2}}, \end{aligned} \tag{4.8}$$

where $\chi(\boldsymbol{x}) = 1$ for an interior point $\boldsymbol{x} \in \Omega_1$ and $\chi(\boldsymbol{x}) = \frac{\mathbf{1}}{\mathbf{2}}$ if $\boldsymbol{x} \in S_1 \cup S_2$. In the boundary element method, both $\boldsymbol{x}$ and $\boldsymbol{x}'$ are on $S_1 \cup S_2$. We can discretize the equation (4.7) using matrices defined below (see Figure 4b for symbols):

$$\begin{aligned} \mathrm{T}^{(11)}(I,I') &= \iint_{\Sigma_{I'}^{(1)}} \mathrm{C_{ijkl}}(\mathbf{x}')\mathrm{G_{kn,l}}(\mathbf{x}',\mathbf{x}_\mathrm{I},\omega)\mathrm{n_j^{(1)}} \mathrm{d}\mathbf{x}'^{\mathbf{2}}, \mathbf{x}' \in \Sigma_{I'}^{(1)}; \\ \mathrm{T}^{(12)}(I,J') &= \iint_{\Sigma_{J'}^{(2)}} \mathrm{C_{ijkl}}(\mathbf{x}')\mathrm{G_{kn,l}}(\mathbf{x}',\mathbf{x}_\mathrm{I},\omega)(-\mathrm{n_j^{(2)}}) \mathrm{d}\mathbf{x}'^{\mathbf{2}}, \mathbf{x}' \in \Sigma_{J'}^{(2)}, \end{aligned} \tag{4.9}$$

$$\mathrm{G}^{(12)}(I,J') = \iint_{\Sigma_{J'}^{(2)}} \mathrm{G}_{\mathrm{in}}(\mathbf{x}', \mathbf{x}_{\mathrm{I}}, \omega)\mathrm{d}\mathbf{x}'^{\mathbf{2}}, \mathbf{x}' \in \Sigma_{J'}^{(2)},$$

$$\mathrm{T}^{(21)}(J,I') = \iint_{\Sigma_{I'}^{(1)}} \mathrm{C}_{\mathrm{ijkl}}(\mathbf{x}')\mathrm{G}_{\mathrm{kn,l}}\left(\mathbf{x}', \mathbf{x}_J, \omega\right)\mathrm{n}_{\mathrm{j}}^{(1)}\mathrm{d}\mathbf{x}'^{\mathbf{2}}, \mathbf{x}' \in \Sigma_{I'}^{(1)},$$

$$\mathrm{T}^{(22)}(J,J') = \iint_{\Sigma_{J'}^{(2)}} \mathrm{C}_{\mathrm{ijkl}}(\mathbf{x}')\mathrm{G}_{\mathrm{kn,l}}\left(\mathbf{x}', \mathbf{x}_J, \omega\right)(-\mathrm{n}_{\mathrm{j}}^{(2)})\mathrm{d}\mathbf{x}'^{\mathbf{2}}, \mathbf{x}' \in \Sigma_{J'}^{(2)},$$

$$\mathrm{G}^{(22)}(J,J') = \iint_{\Sigma_{J'}^{(2)}} \mathrm{G}_{\mathrm{in}}\left(\mathbf{x}', \mathbf{x}_J, \omega\right)\mathrm{d}\mathbf{x}'^{\mathbf{2}}, \mathbf{x}' \in \Sigma_{J'}^{(2)}.$$

We can obtain the final form of discretized boundary integral equations system for solid-liquid core model by combining BIE in both liquid and solid medium:

$$\begin{aligned}
\frac{1}{2}\left[\mathrm{u}^{(1)}\right] &= \left[\mathrm{u}_0^{(1)}\right] - \mathrm{T}^{(11)}\left[\mathrm{u}^{(1)}\right] - \mathrm{T}^{(12)}\left[\mathrm{u}^{(2)}\right] + \mathrm{G}^{(12)}\left[\mathrm{t}^{(2)}\right], \\
\frac{1}{2}\left[\mathrm{u}^{(2)}\right] &= \left[\mathrm{u}_0^{(2)}\right] - \mathrm{T}^{(21)}\left[\mathrm{u}^{(1)}\right] - \mathrm{T}^{(22)}\left[\mathrm{u}^{(2)}\right] + \mathrm{G}^{(22)}\left[\mathrm{u}^{(2)}\right], \\
\frac{1}{2}[\mathrm{P}] &= [\mathrm{P}_0] - \mathrm{A}[\mathrm{P}] + \mathrm{B}[\mathrm{q}],
\end{aligned} \tag{4.10}$$

where $\left[u^{(1)}\right]$ is a vector containing the 3-component surface displacements for the elements on S_1. Similarly, $\left[u^{(2)}\right]$ is a vector containing the 3-component surface displacements for the elements on S_2, $\left[t^{(2)}\right]$ is the column traction vector on S_2. $\left[u_0^{(1)}\right]$ and $\left[u_0^{(2)}\right]$ are vectors containing the incident field for the elements on S_1 and S_2, respectively. $[P]$ is a vector containing the pressure field for the elements on S_1. $[P_0]$ is a vector containing incident pressure field for the elements on S_2. By including boundary condition on the solid-liquid boundary:

$$\begin{aligned}
\frac{\partial \mathrm{P}(\mathbf{x})}{\partial \mathbf{n}^{(2)}(\mathbf{x})} &= \rho\omega^2 \mathbf{u}^{(2)}(\mathbf{x}) \cdot \mathbf{n}^{(2)}(\mathbf{x}), \mathbf{x} \in \mathrm{S}_2, \\
\mathbf{t}^{(2)}(\mathbf{x}) &= \mathrm{P}(\mathbf{x})\mathbf{n}^{(2)}(\mathbf{x}), \mathbf{x} \in \mathrm{S}_2\ ,
\end{aligned} \tag{4.11}$$

where $\mathbf{n}^{(2)}(\boldsymbol{x})$ is the surface normal at $\boldsymbol{x}$ on S_2, $\boldsymbol{t}^{(2)}$ is the surface traction in the solid region on S_2. We can now solve equation (4.10) for $\boldsymbol{u}^{(1)}$, $\boldsymbol{u}^{(2)}$, and $P(\boldsymbol{x})$ which are the field values on the boundaries. Finally, we can use equations (4.6) and (4.8) to calculate the displacement wavefield at any interior point in Ω_1 or Ω_2.

For BEM modeling mesh building, I first partition the surface by creating an approximately uniform triangular tessellation on a unit sphere by minimizing generalized electrostatic potential energy of a system of charged particles using the code by Semechko (2015). We can magnify or shrink the unit sphere mesh to any size we need. We can also directly add the height of the topography to the vertex of the mesh to achieve topography on our model. To implement surface integration on a boundary element (e.g., equations (4.7) and (4.9)), I use quadrature integration using a MATLAB program from Xiao and Gimbutas (2010).

4.2 Benchmark of BEM

4.2.1 Benchmark example 1 - Homogenous solid sphere with a single force source

First, I benchmark the seismic wavefield caused by a single force source in a 3D homogenous elastic and spherical solid. I set the compressional wave velocity as $v_p = 6km/s$ and the shear wave velocity $v_s = 3$ km/s. I set the density as $3000\ kg/m^3$. The spherical body is 20km in radius without topography. The single force source is given as $\boldsymbol{f} = [1,1,1]N$. The location of the source is at depth of 10km, 180° in longitude and 0° in latitude (Figure 5a). I also included attenuation by applying Q values for the P and S wavenumbers,

$$\mathrm{k}_\alpha = \frac{\omega}{\mathrm{v_p}}\left(1 + \frac{i}{2\mathrm{Q_p}}\right),$$
$$\mathrm{k}_\beta = \frac{\omega}{\mathrm{v_s}}\left(1 + \frac{i}{2\mathrm{Q_s}}\right), \tag{4.12}$$

where ω is the angular frequency. The S-wave attenuation is given as $Q_s = 200$ and the P wave attenuation is given as $Q_p = 2.5Q_s$. To avoid the wrap-around effect (Bouchon *et al.*, 1989), I add an imaginary part to the angular frequency, $\omega \rightarrow (\omega + \frac{i}{T_m})$, where T_m is the duration of the recording.

I generate a mesh for BEM for the spherical elastic body with a radius of 20km (Figure 5b).

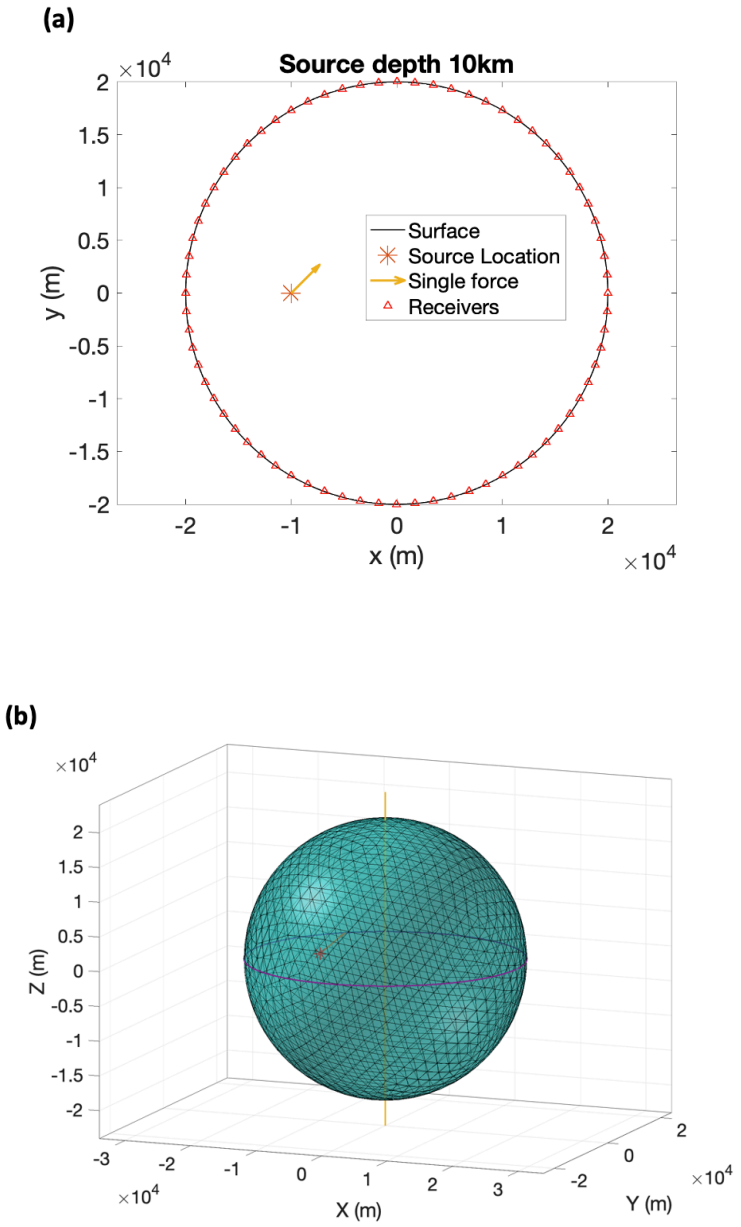

Figure 5. A Homogenous model with a single-force source. (a) The source and receivers are on the equatorial plane. The solid body is 20 km in radius. We placed the source (indicated by a red star) at depth of 10 km, 180° in longitude and 0° in latitude. The direction of the force is given by the yellow arrow. All the receivers are placed on the equator, spaced at an interval of 5°. (b) 3D view of the boundary mesh. The red star is the source location. The blue circle in the middle is the equator. The yellow line is the axis through the poles.

Using the AstroSeis code, we can model the surface seismic displacement. I compare the modeled seismogram of AstroSeis with that of the normal mode summation method for the

single force source. I find that the root-mean-squares (RMS) error of the waveform difference is only 0.88% (Figure 6).

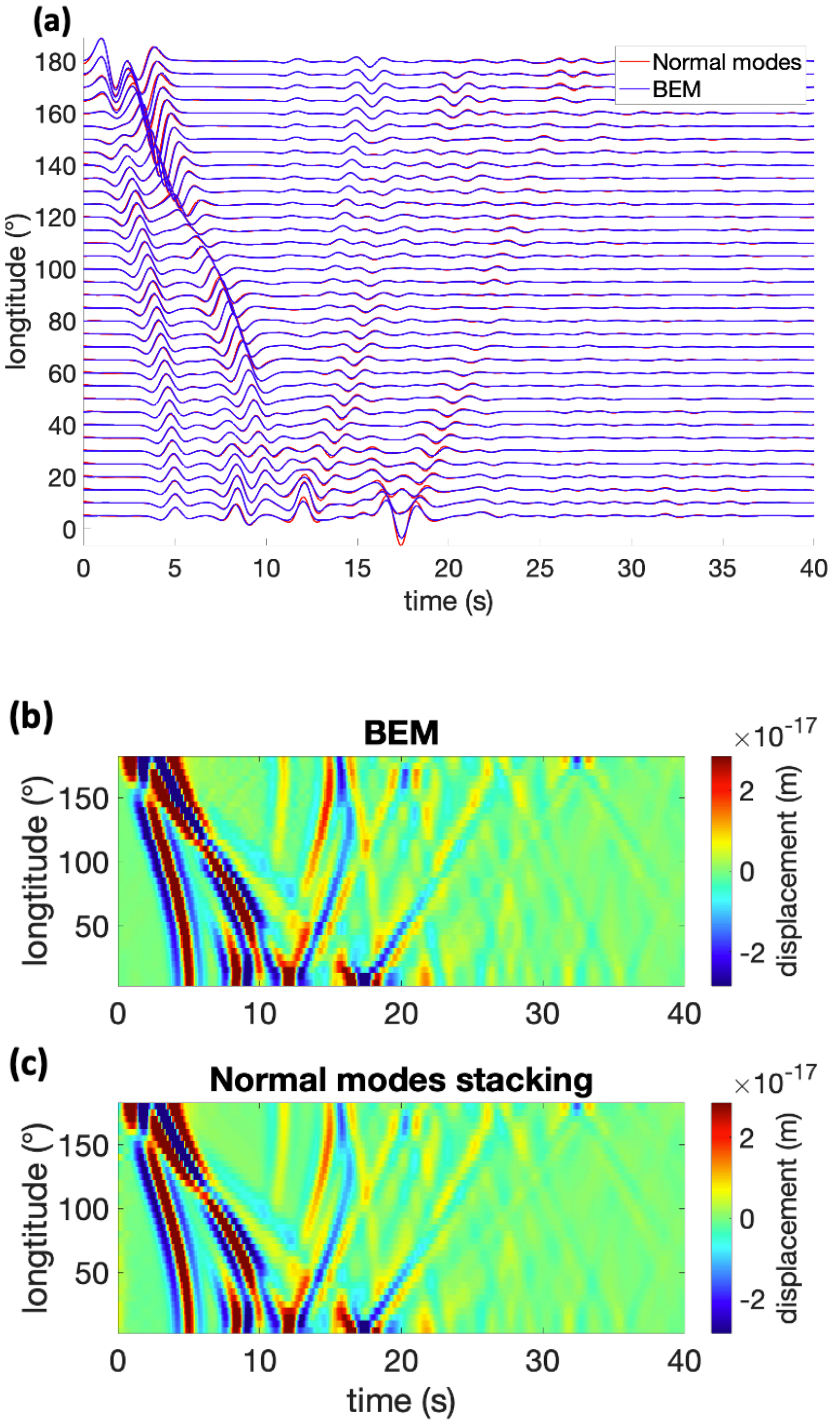

Figure 6 Seismic displacement (vertical component) waveform of the model in Figure 5 using two different methods: BEM and normal modes summation, for a single force source. (a) Wiggle-to-wiggle comparison of seismic waveforms due to a single force source shown in Figure 5. (b) A common source gather by BEM; (c) Common source gather by the normal mode summation method.

4.2.2 Benchmark example 2- Homogenous solid sphere with explosion source

To test whether the AstroSeis code can work with an explosion source, I use the same model as in Figure 5. I only change the source to an explosion source (Figure 7). The moment tensor of the explosion source is given as $M = \begin{bmatrix} 1 & 0 & 0 \\ 0 & 1 & 0 \\ 0 & 0 & 1 \end{bmatrix} N \cdot m$. By comparing the BEM result with the normal mode summation method, the RMS error of the waveform difference is only 0.48% (Figure 8).

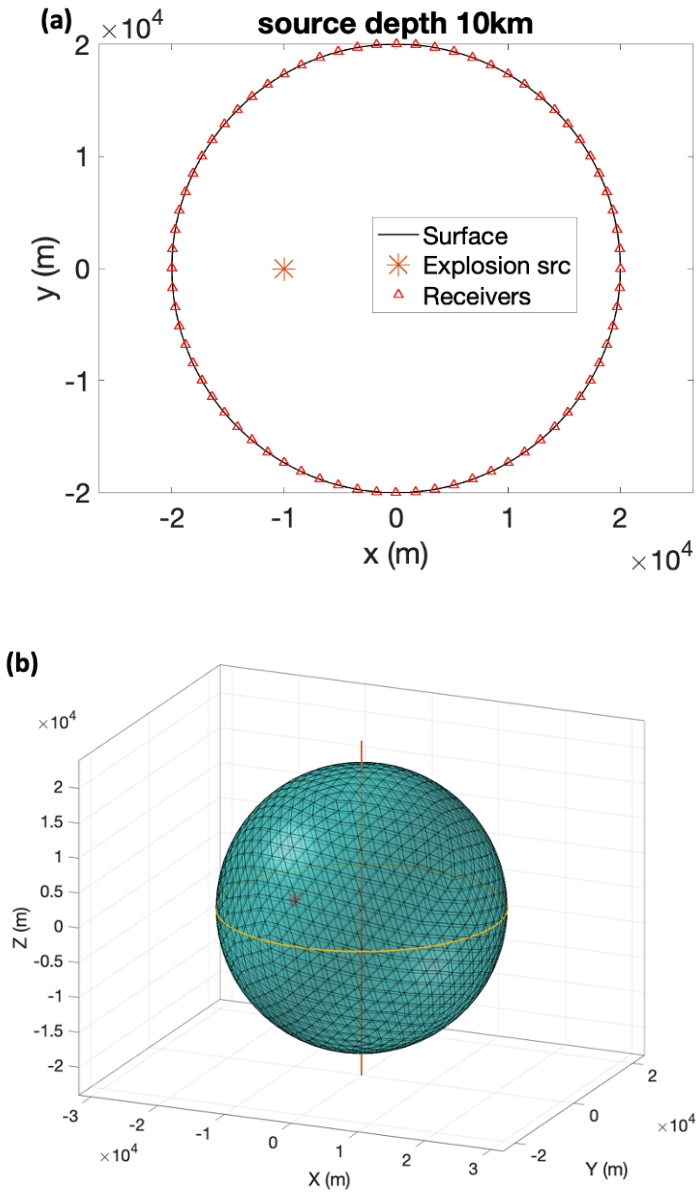

Figure 7 An explosion source in a homogeneous model. (a) The source and receivers are on the equatorial plane. The solid body is 20 km in radius. We placed the source indicated by a red star at depth of 10 km, 180° in longitude and 0° in latitude (on the equator plane). All the receivers are also placed on the equator, spaced at an interval of 5°. (b) 3D view of the boundary mesh. The red star is the location of the source. The orange circle is the equator. The red line is the axis through the poles.

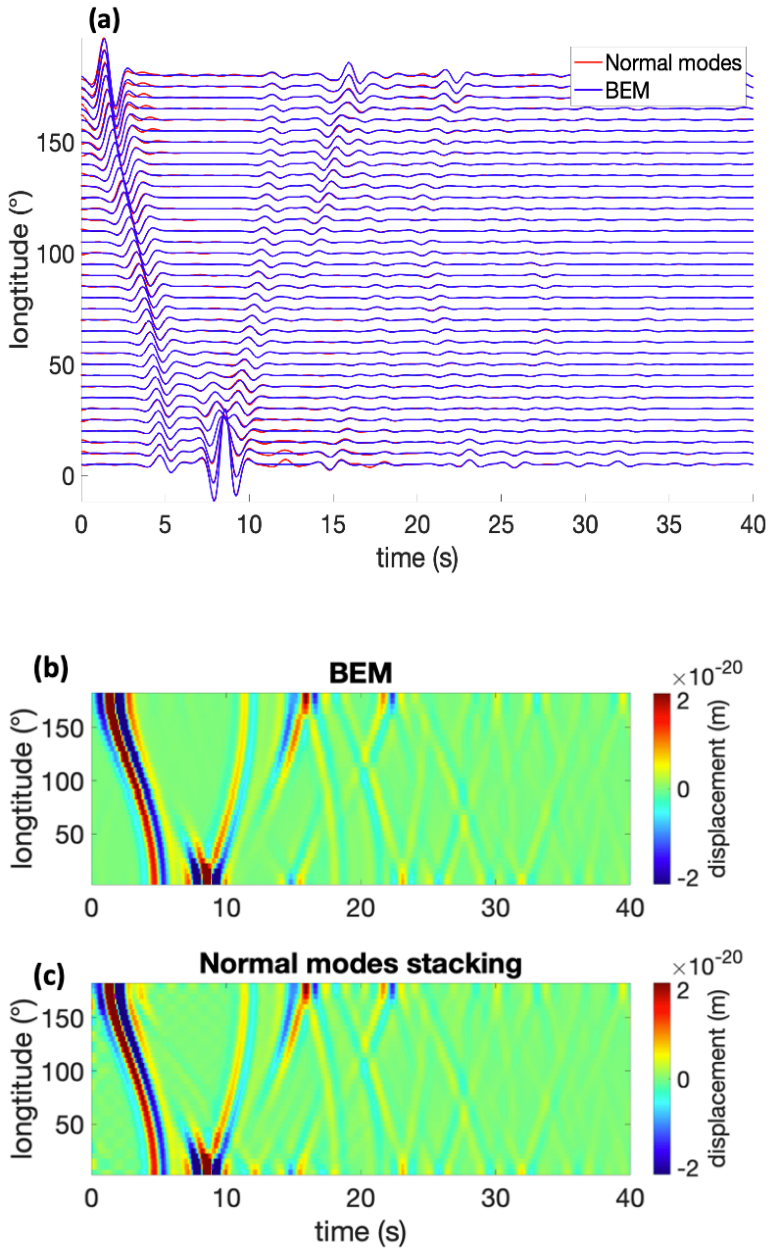

Figure 8 Seismic displacement fields (vertical component) for the model in Figure 7 computed by BEM and the normal mode summation for an explosion source. (a) Wiggle-to-wiggle comparison of seismic waveforms due to an explosion source shown in Figure 7. (b) Common source gather computed by BEM; (c) Common source gather by the normal mode summation method.

4.2.3 Benchmark example 3 - Solid sphere with a liquid core

In the third example, I benchmark the code for a liquid core model (Figure 9). The source is the same explosion source used in example 2. The solid medium is the same as the model in example 1 and 2. The liquid part has a compressional wave velocity of 8 km/s, and density

is 4000 kg/m^3. I calculated seismic wavefields using our BEM and DSM. These results also show good agreement and the RMS error of the waveforms difference between the two methods is 1.45% (Figure 10).

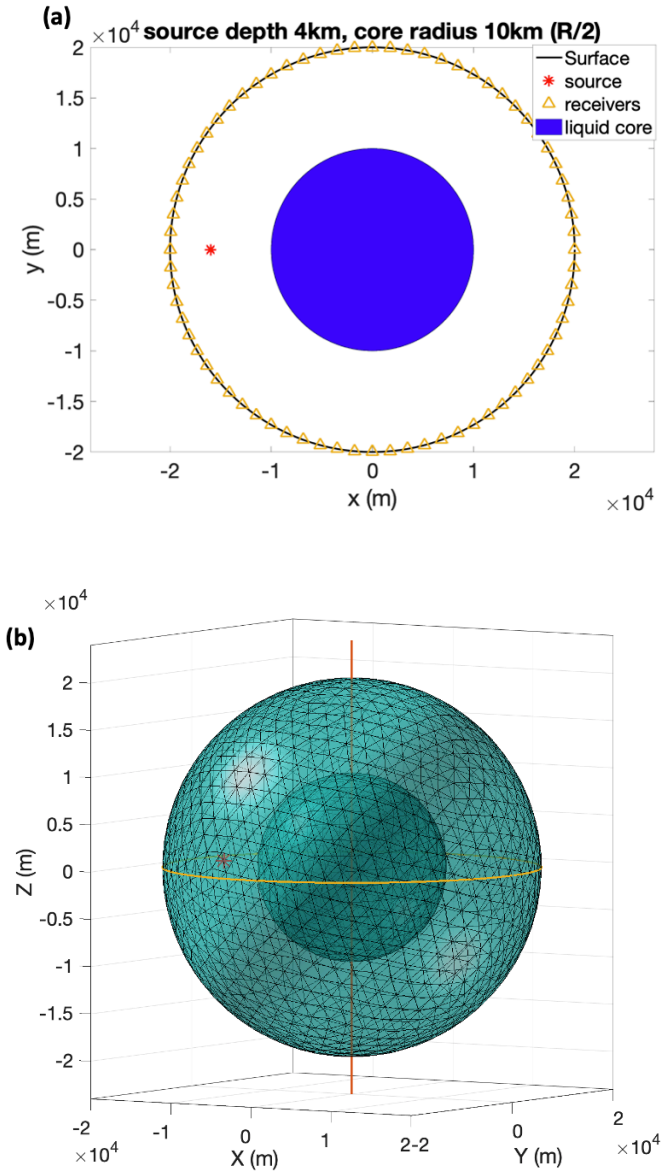

Figure 9 A solid sphere with a liquid core model with an explosion source. (a) The source (red star) and receivers (orange triangles) shown on the equatorial plane. The solid body is 20 km in radius. The liquid core is 10km in radius. We placed the source at depth of 4km, 180° in longitude and 0° in latitude (on the equator plane). All the receivers are on the equator, spaced at an interval of 5°. (b) 3D view of the boundary mesh. The red star is the location of the source. The orange circle is the equator. The red line is the axis through the poles.

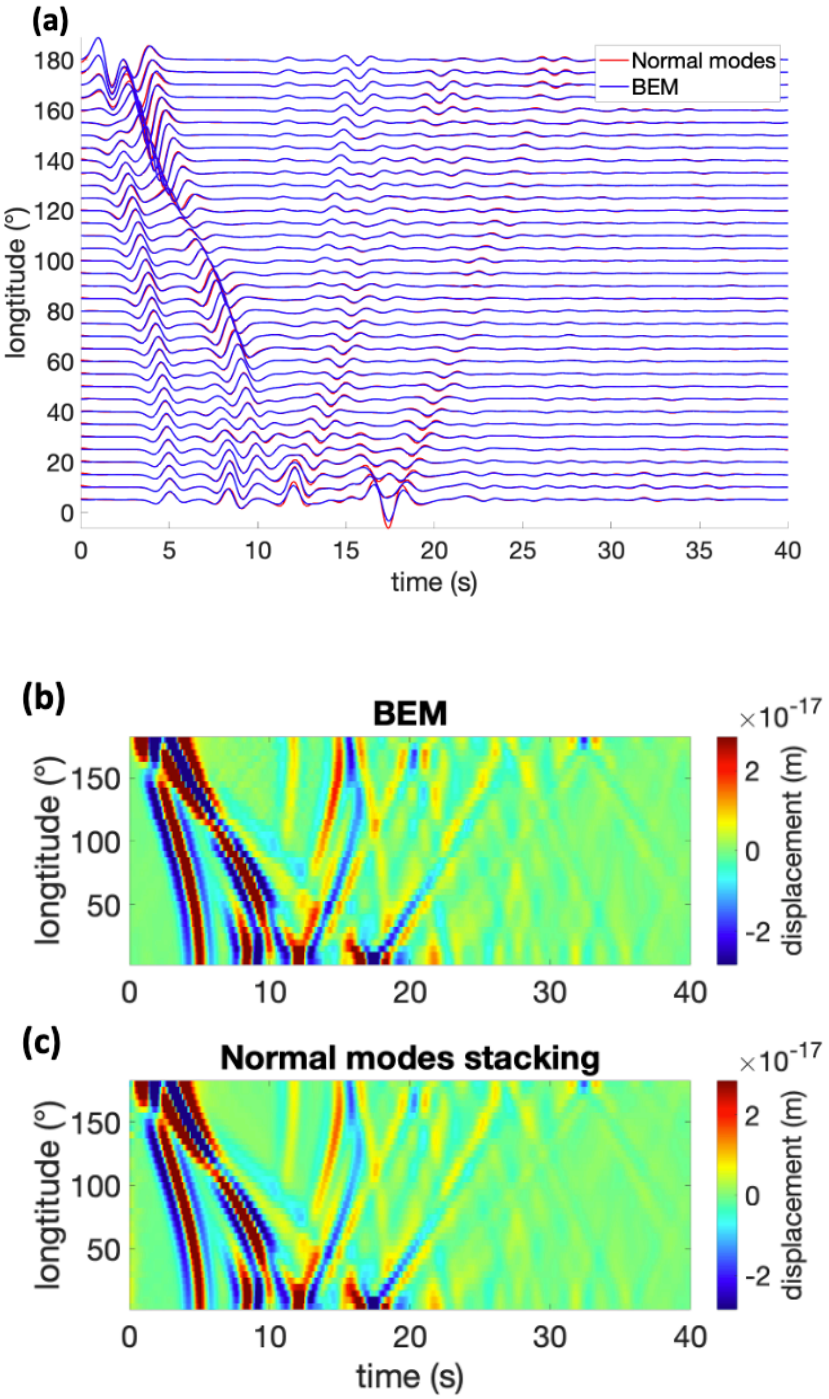

Figure 10 Seismic displacement (vertical component) comparison between BEM and DSM for an explosion source. (a) Wiggle-to-wiggle comparison of seismic waveforms (BEM versus DSM). (b) Common source gather by BEM; (c) Common source gather by DSM (Kawai et al., 2006).

4.3 Numerical examples

Here, I show several numerical examples that I can compute with the proposed codes. First, I show that our code can model seismic wavefield for a body with a liquid core at an arbitrary location.

Second, I show that I can model seismic wavefield in Phobos with its real topography (Willner *et al.*, 2014).

4.3.1 Shifted-core model

I can use the BEM code to model the seismic wavefields in two models: a solid body with a liquid core (the centered-core model), and a solid body with a shifted core. In the shifted-core model, the core is shifted along the y-direction by 2km from the center (Figure 11a). I use AstroSeis to compute seismic displacement (vertical component) wavefields in these two models (Figure 11b). We can clearly see a lack of focusing for the seismic field at the antipode caused by the shift of the core (Figure 11c).

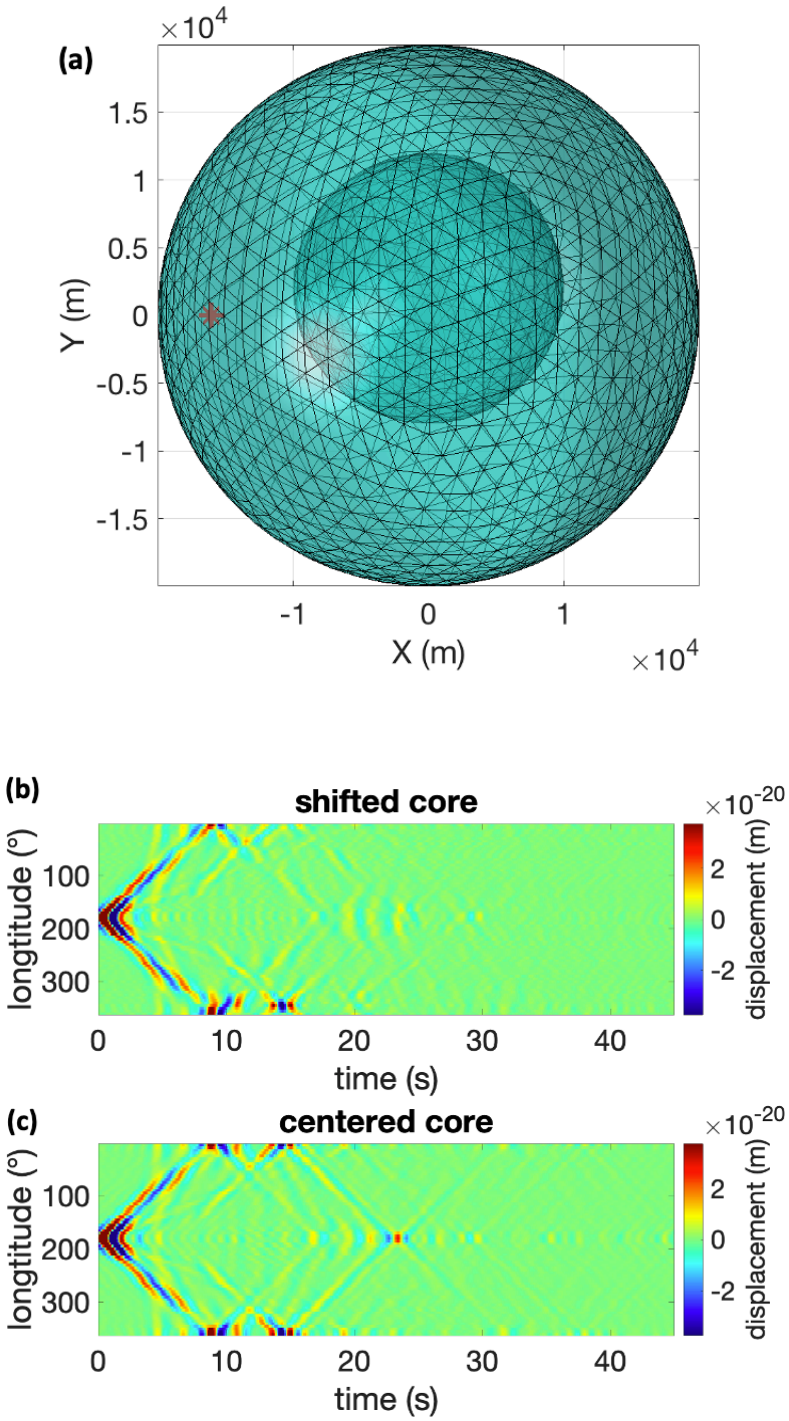

Figure 11 The seismic wavefield (vertical displacement) in a solid sphere with a shifted liquid core. (a) The mesh of a solid sphere with a shifted liquid core to calculate seismic displacement wavefield. The core is shifted along the y direction by 2km. The explosion source is given as an identity matrix. The source location is indicted by a red star, at a depth of 4 km, 180° in longitude, and 0° in latitude (on the equator plane). All the receivers are placed on the equator at an interval of 5°. In this solid medium, we set the compressional wave velocity $v_p = 6\ km/s$ and the shear wave velocity $v_s = 3$ km/s, the density $\rho = 3000\ kg/m^3$; in the liquid medium, we set compressional wave velocity $v_p = 8000\ m/s$, density $\rho = 4000\ kg/m^3$. (b) Common source gather for the shifted-core model in (a). (c) Common source gather from a solid sphere with a centered liquid core (i.e., no shift).

4.3.2 Seismic modeling for Phobos

In this example, we model seismic fields in Phobos, the closer moon of Mars. Phobos has a very irregular topography (Figure 12a). I compute the seismic displacement wavefield of Phobos with an explosion source at depth of 4km on the Phobos' equator plane (Figure 12b). To see how topography modifies the seismic wavefield, I also compute the seismic field for a homogenous spherical model with a similar size. We can observe that topography has greatly changed the vertical component seismic displacement wavefield.

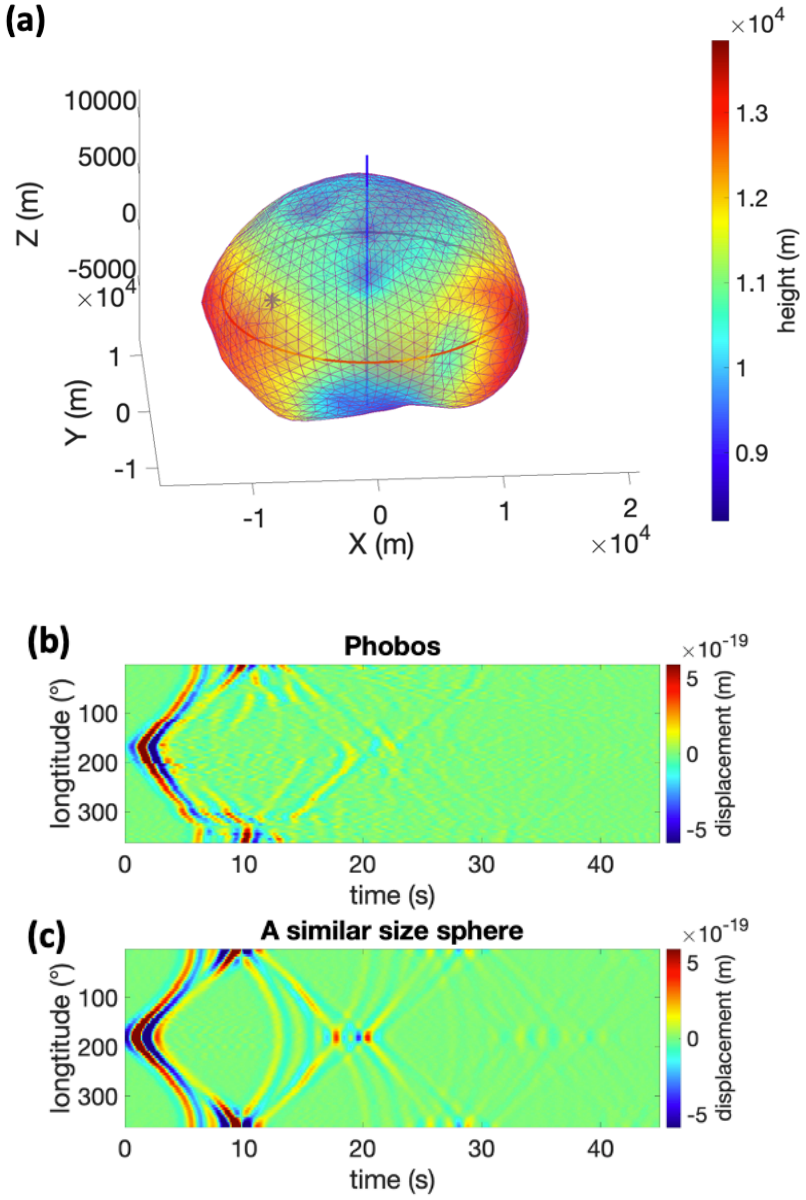

Figure 12. Seismic wavefield in Phobos. (a) The topography model of Phobos with the surface mesh. We define the positive x-axis is 0° in longitude, the positive y-axis is 90° in longitude. The source location is indicated by a blue star, at depth of 4km, 180° in longitude and 0° in latitude (on the equatorial plane). All the receivers are placed on the approximated equator with an interval of 5°. In this model, I set the compressional wave velocity $v_p = 3\ km/s$ and the shear wave velocity $v_s = 1$ km/s, the density $\rho = 1880\ kg/m^3$. And the explosion source is given as an identity matrix. (b) Common source gather from the model shown in (a). (c) Common source gather from an elastic sphere with 10.9 km in radius.

4.3.3 Seismic exploration of Phobos

Because of the complex topography features of Phobos, I analyze the seismic displacement wavefield at different frequencies to investigate whether certain topography features can be

excited (Figure 13). I use the same model and source location as shown in Figure 12. The source is at depth of 4km and a longitude of 180°. The source is a monofrequency source/shaker. We can observe that the pronounced topography feature, Stickney crater, has a strong response and 'resonates' at ~0.18Hz for the P- and S-wave speeds used in the modeling. The P- and S-wave velocities are very important to understand the asteroid internal structure. Unfortunately, they unknown in asteroids. However, we can use this resonance phenomenon to constrain the seismic wave speeds. We can burrow a shallow hole in Phobos and deploy a seismic shaker into it to actuate vibrations at any frequency we want. In the meantime, we place a seismic sensor at the rim of the Stickney crater, we can study the frequency dependent seismic displacement field to determine the average P and S wave speeds for Phobos. The seismic sensor could also be an optical fiber.

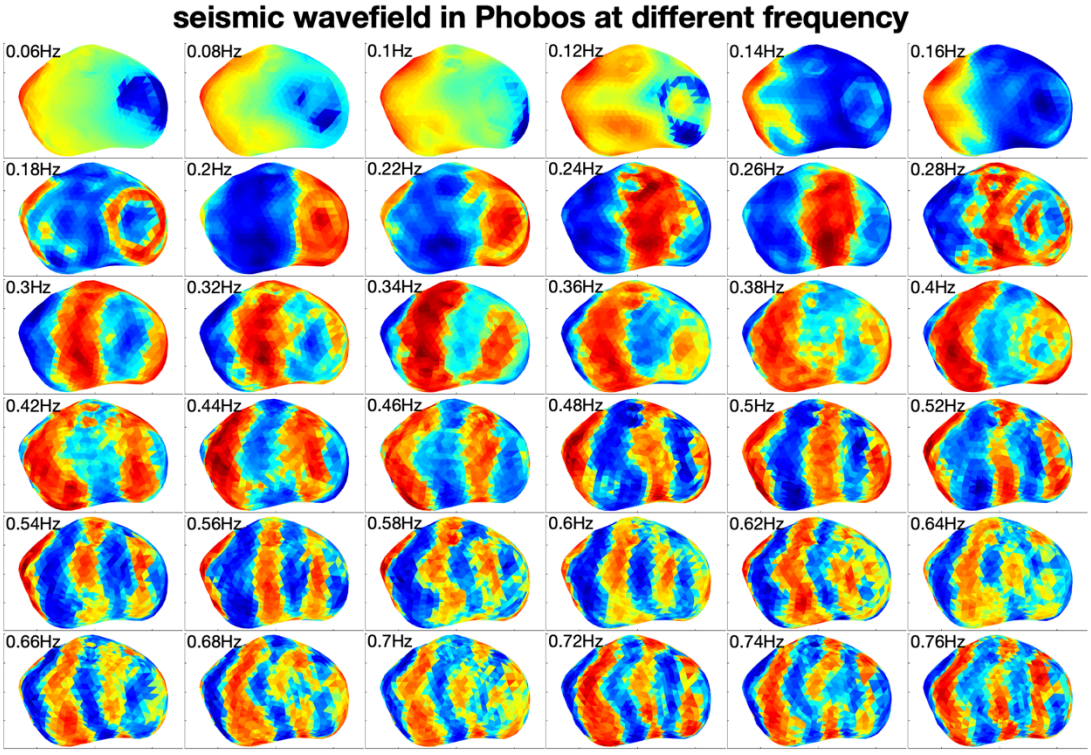

Figure 13 Snapshot of modeled seismic wavefield patterns on the surface of Phobos at different frequencies. The value shown (red/blue color) is the signed square root of real part of the seismic displacement to enhance contrast for visualization.

4.4 Incident field from tidal force

The conventional way to calculate the tidal deformation using Love numbers have limitations. We can easily calculate Love number for a simple 1-D planet model, but it is hard to analytically calculate Love number for 3-D models or models with topography which is known for affecting tidal response. We can use BEM to solve this problem numerically. To apply BEM, we need to calculate the incident field using tidal force.

The incident field on a planet, $u_{0q}(\mathbf{x},\omega)$, excited by the tidal force of a moon orbiting the planet (see equation (2.1)) along the q -th direction in the frequency domain can be computed as:

$$u_{0q}(\mathbf{x},\omega) = \iiint_V \rho(\mathbf{x}')\mathrm{g_i}(\mathbf{x}',\omega)G_{iq}(\mathbf{x},\mathbf{x}',\boldsymbol{\omega})d\boldsymbol{x}'^{\mathbf{3}}, \tag{4.13}$$

where $\mathbf{x}$ and $\mathbf{x}'$ are points in the planet, V is the space occupied by the planet. $G_{iq}(\mathbf{x},\mathbf{x}',\omega)$ is the Green's function in a homogeneous unbounded elastic medium. $\mathrm{g}_i(\mathbf{x}',\omega)$ is the tidal force of the moon at $\mathbf{x}'$ along the i-th direction in the frequency domain. The value of $\mathrm{g}_i(\mathbf{x}',\omega)$ at each frequency is the Fourier coefficient of equation (2.1):

$$\mathbf{g}(\mathbf{x}',\omega) = \frac{1}{T}\int_0^T \boldsymbol{g}(\mathbf{x}',t)e^{i\omega t}dt \tag{4.14}$$

where T is the orbital period. The frequency ω takes discrete values ($n\omega_0$) as shown section 2.1, where $n = 1,2,3$ .... Once we have u_0 as the incident field, we can insert it into equation (4.1) to perform the BEM modeling. The surface displacement wavefields will be solved numerically.

4.5 Summary

I have presented the theory and developed a numerical seismic modeling package, AstroSeis, based on the boundary element method. This package can handle complex arbitrary surface topography, solid-liquid interfaces, frequency-dependent seismic attenuation, and various source types such as a single force or a moment tensor source. I have verified the validity of the code with the analytical solution (normal mode summation) for a homogenous solid model. I have also benchmarked the code against DSM for modeling seismic waves for a liquid core model. I showed the capability of the code in modeling seismic waves in Phobos. I expect this code will be a useful tool in future seismic exploration for asteroids and other planets. Besides, we can use this code to calculate surface deformation of a planet induced by an orbiting moon. We can further calculate the tidal torque on the moon from the surface deformation

Chapter 5 Tidal torque and orbital decay rate

An orbiting moon exerts a cyclic tidal force for every point in the planet. Therefore, this tidal force can cause seismic displacement in the planet, which leads to the deformation of the planet. The change of the figure of the planet can alter the planet's gravitational field to exert a net torque on the moon. I use the boundary element integral equation approach (Zheng *et al.*, 2015) (also see Chapter 4) to compute the deformation of the planet caused by the tidal force from the moon. To focus on the tidal-seismic resonance effect, I did not consider the effect of gravity on the propagation of the seismic wave (Dahlen and Tromp, 1998) in my calculation. Once we obtain the seismic wavefield, we can compute the time-dependent torque on the moon and the orbital decay rate of the moon. To verify the proposed numerical approaches, I compare the numerical torque results with the analytical torque calculation for a homogeneous planet model. I find that the two results are in excellent agreement.

5.1 Methods

5.1.1 Numerical torque from BEM

Once we obtain seismic displacement, $\mathbf{u}(\mathbf{x},t)$ from BEM, we can calculate the excessive mass on the surface of the planet caused by the tidal force. The excessive mass will exert a time-t dependent torque on the moon:

$$\boldsymbol{M}(t) = \oiint \rho \boldsymbol{r}_m(t) \times G m_m \frac{\mathbf{x} - \mathbf{x}_m(t)}{|\mathbf{x} - \mathbf{x}_m(t)|^3} [\mathbf{u}(\mathbf{x}, \mathrm{t}) \cdot \mathbf{e}_\mathrm{r}] d\mathbf{x}^2, \tag{5.1}$$

where, $\mathbf{x}_m$ is the location of the orbiting moon; ρ is the density of the planet; and $\boldsymbol{e}_r$ is the surface normal at **x**.

We can derive the orbital decay rate of the moon ($\dot{r}_m(t) = dr_m(t)/dt$) by using Newton's second law:

$$|\dot{r}_m(t)| = \frac{2\left|\overline{\boldsymbol{M}(t)}\right|}{m_{\text{moon}}}\sqrt{\frac{\mathrm{r_m(t)}}{Gm_{pl}}}, \tag{5.2}$$

where $\overline{\mathbf{M}(t)}$ is the average torque on the moon in one orbital period, G is the universal gravitational constant, m_{moon} is the mass of the moon, and m_{pl} is the mass of the planet.

I have shown that both $\mathbf{g}[\mathbf{x},t]$ and $\mathbf{u}(\mathbf{x},t)$ are proportional to the mass of the moon in Chapter 2. In equation (5.2), the orbital decay rate is divided by the mass of the moon m_{moon}. Therefore, the orbital decay rate is proportional to the mass of the moon. If the mass of the moon changes, the orbital decay rate will change accordingly.

5.1.2 Analytical torque from Love number

The tidal torque Γ can be computed as (p.164 of Murray and Dermott, 1999):

$$\Gamma = \frac{9}{10}h_2\frac{Gm}{r_p}\left(\frac{a}{r_p}\right)^5 \sin 2\varepsilon, 2\varepsilon = Q^{-1}, \tag{5.3}$$

where m is the mass of the moon, r_p is the moon's orbit radius, and Q is the shear quality factor, ε is the lagging angle.

5.2 Comparison between analytical torque and BEM numerical torque

Since the proposed BEM modeling does not consider the self-gravitation of the planet, I need to use the Love number under the same condition. In Chapter 2, I calculated the analytical tidal Love number using equation (2.17), (2.21) and obtained $h_2 = h_2^* = 0.5877$ for a planet with a 2000km radius, a compressional wave velocity of $v_p = 3$ km/s, a shear wave velocity of $v_s = 1.2$ km/s, and a density of 2840 kg/m^3. The numerical torque calculation using equation (5.1), based on the boundary element modeling and the same planet model, agrees well with the analytical calculation based on h_2^* (Figure 14). We expect discrepancies at low orbit heights (Figure 14), because the tidal potential is no longer degree 2.

I also note that the torque is inversely proportional to Q. As expected, we see a factor of 4 for the numerical torque values for two different Q values, Q=50 and Q=200, at the same orbit radius.

5.3 Summary

In this chapter, I have proposed a numerical way to calculate the tidal torque from the surface deformation. I have verified the result with the analytical torque.

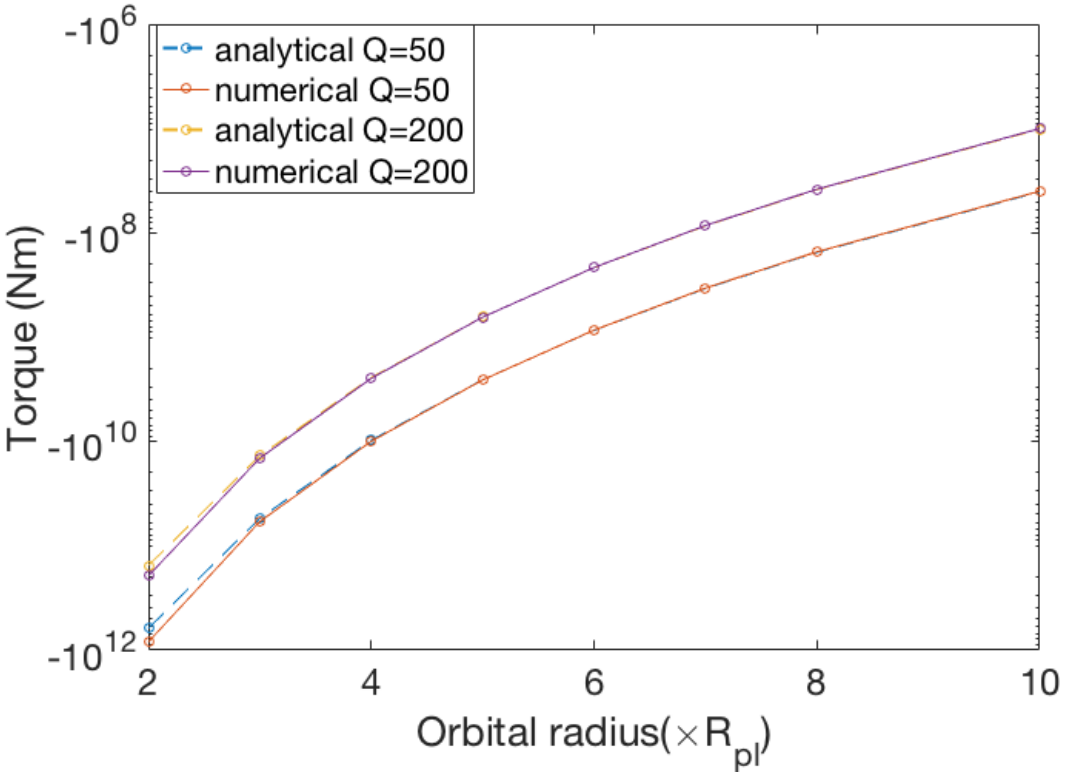

Figure 14. Comparison of analytical torque and numerical torque (based on the boundary element modeling, see equation (5.1) for different orbital radii and Q values. The analytical torque is computed using equation (2.21) and (5.3) with $h_2 = 0.5877$. R_{pl} is the planet's radius equal to 2000 km.

Chapter 6 Tidal-seismic resonance

In this chapter, I will introduce a new kind of mechanism between a planet and its moon. Although, an initial idea of this phenomenon had been brought out by Darwin (1898a) more than 120 years ago, I currently can use numerical simulation to predict when it can occur and how it can occur. I name this phenomenon "tidal-seismic resonance". I also show the effect of tidal-seismic resonance, and some potential application of tidal-seismic resonance.

6.1 Model setup

In this analysis, it is better to make some simplifications and approximations to focus on the tidal-seismic resonance effect. We consider a planet-moon system as a binary rotating system in an inertial reference frame. We assume the moon is a point mass and we do not consider potential fragmentation of the moon at the Roche limit (Aggarwal and Oberbeck, 1974; Asphaug and Benz, 1994; Black and Mittal, 2015). The modeled planet does not spin with respect to the reference frame. We assume that the moon's orbit is circular along the planet's equatorial plane. The orbiting period of the moon can be computed using Kepler's laws. I compute the moon's tidal force for every point inside the planet by subtracting the centrifugal force from the gravitational attraction force for the moon.

We consider two planetary models: model-1 with no topography, and model-2 with topography. In model-1, the planet is a homogeneous, elastic, and spherical solid with no topography. I set the compressional wave velocity in the solid as $v_p = 3$ km/s, the shear wave velocity as $v_s = 1.2$ km/s, and the radius of the planet as 2000 km. I use the mass-radius relation (Chen and Kipping, 2017) to set the planet density as $\rho = 2840\ kg/m^3$. For this planet, the shear modulus is low in the model which could represent an icy body known to have low shear modulus (e.g., Nimmo *et al.*, 2007) or a planet with a liquid core which can

effectively lower the entire shear modulus. The mass of the moon is taken as, 10^{16} kg (as a reference, this is similar to the mass of an object like Phobos), which is about 10^{-7} times of the mass of the planet. I consider the effect of *Q,* which captures the dissipation effect of the planet. Previous researchers showed that *Q* could cause a tidal phase lag and was important in calculating the orbital decay of the moon (Zharkov and Gudkova, 1997; e.g., Bills *et al.*, 2005; Nimmo and Faul, 2013; Zheng *et al.*, 2015). I also build a second planetary model of the same material (model-2), but with a randomly generated topography to study how planet topography can also play a role in the tidal-seismic resonance

6.2 When tidal-seismic resonance can happen

To see when the tidal-seismic resonance can occur, we can compute the planet's normal-mode frequencies and tidal force frequencies. Because the moon orbits around the planet periodically, the tidal force is periodic at any point in the planet. If the orbital frequency is designated as ω_0, we also expect to see higher-order harmonics such as $n\omega_0$ where n=2, 3, 4, …. The tidal-seismic resonance occurs when a tidal force frequency is the same as a normal-mode frequency (Figure 15). The tidal force preferentially excites the fundamental spheroidal normal mode, ${}_0S_n$, where *n* is the degree in the surface spherical harmonic function.

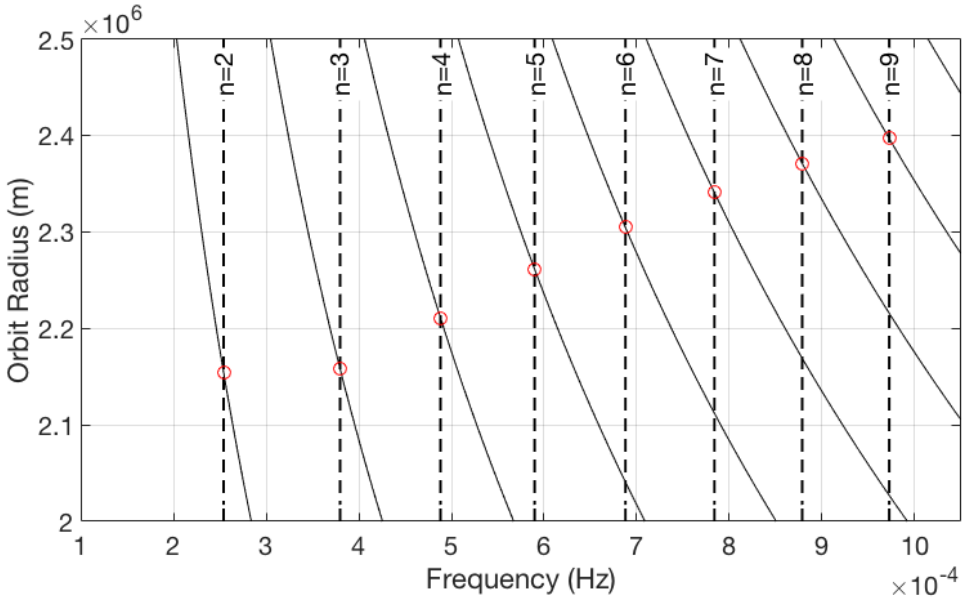

Figure 15. Tidal force and planet normal mode frequencies for model-1. The solid lines are tidal force frequencies calculated for a point on the planet equator. The vertical dashed lines are the planet free-oscillation frequencies for the spheroidal ${}_0S_n$ normal modes (n=2, 3, 4, …). The tidal-seismic resonance occurs when tidal force frequencies intersect the planet free oscillation frequencies at the red circles.

6.3 Effect of tidal-seismic resonance

6.3.1 Tidal-seismic resonance at low orbits

At low orbits, we observe that the orbital decay rate overall increases as the moon approaches the planet and the that the tidal seismic effect punctuates/accelerates this trend locally at several distinct orbital radii ("peaks" in Figure 16). The locations of the "peaks" correspond to special orbital radii at which tidal-seismic resonance exerts a strong on the orbiting moon. Because of their uncommon significance, we call these orbital radii r_n^*, where $n = 2, 3$ .... At r_n^*, the planet ${}_0S_n$ normal mode frequency is exactly n times the moon's orbital frequency. In these cases, both the tidal force and the ${}_0S_n$ mode have degree-n spatial patterns within the planet. Therefore, it is a simultaneous coupling for both the temporary and spatial frequencies (i.e., degree-n) at r_n^*, which can cause a very strong excitation of seismic displacement inside the planet (Figure 16).

I then compute orbital decay rates for several different Q values (see section 5.2). In general (i.e., no tidal-seismic resonance), the decay rate is small if Q is large because the tidal phase lag proportional to 1/Q is small (see Bills et al., 2005). However, at r_n^* where tidal-seismic resonance happens, the opposite is true because a large Q yields a large induced seismic displacement, which gives a large torque and causes a large decay rate (Figure 16). Among all r_n^*'s, the r_2^* is special. At r_2^* where the degree-2 normal mode (i.e., the gravest "football-shaped" mode) is excited by the tidal force, the orbital decay rate is computed and found to be on the order of ~1-10 cm/s for different Q values (Figure 16) for this particular planet/moon model (i.e., model-1) considered here. At the tidal-seismic resonance orbit, the orbital decay rate is 2 orders of magnitude more than that for a neighboring orbit that has no resonance.

I note that the exact numerical value for orbit decay may vary from model to model. However, the tidal-seismic resonance can significantly accelerate the orbital decay ("peaks" in Figure 16 compared to the smooth background trend). The greater the Q value is, the sharper the peaks are. To verify whether these peaks are indeed caused by the tidal-seismic resonance effect, I analytically calculate the normal mode ${}_0S_n$ frequencies of the planet (See chapter 3). I then calculate the corresponding r_n^* whose orbital frequency is $1/n$ times that of the ${}_0S_n$ frequency. I found that the calculated r_n^* based on the ${}_0S_n$ frequency corresponds to the "peaks" of the moon orbital decay rate (Figure 16). In conclusion, the rapid falling of the moon is caused by the tidally excited seismic normal modes of the planet. When the moon's orbit radius is large (e.g., $>2.5 \times 10^6$ m or $> 1.25\ R_{pl}$), the tidal-seismic resonance effect is not pronounced. In this case, a smaller Q value gives a larger orbital decay rate which is consistent with the tidal drag due to the anelasticity effect (Bills *et al.*, 2005).

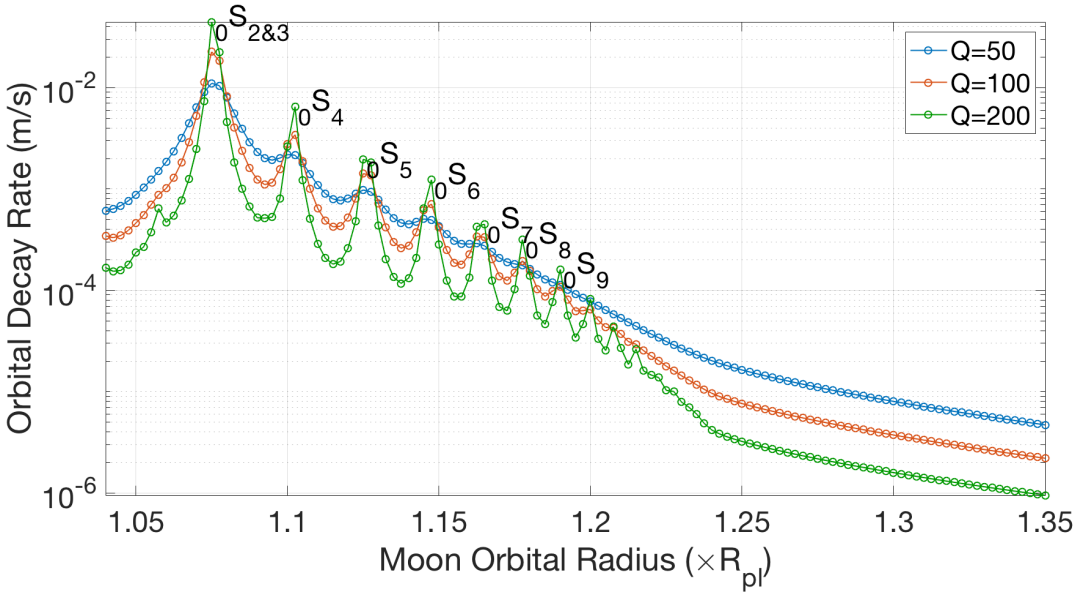

Figure 16. Calculated moon orbital decay rates at different orbital radii and for different Q values for model-1. The horizontal axis is the radius of the moon orbit. The radius of the planet R_{pl} is 2×10^6m. I also label excited normal modes, ${}_0S_n, n > 2$, expected to be seen for the tidal-seismic resonance.

6.3.2 Topography induced tidal-seismic resonance

At higher orbits (orbital radius greater than $2.5 \times 10^6\ m$ or $1.25\ R_{pl}$ in this case), the tidal seismic resonance can occur when $m\omega_0$ matches the ${}_0S_n$ frequency, where both *m* and *n* are integers and typically $m > n$.

In principle, a degree-*m* tidal force field cannot excite degree-n normal mode for a purely spherical and homogeneous planet (i.e., model-1) because these two fields are orthogonal to each other in space. However, if the planet is not spherical (i.e., model-2), the tidal-seismic resonance can still exist because topography could couple modes of different spatial degrees. My purpose here is to investigate the topography-induced tidal-seismic effect.

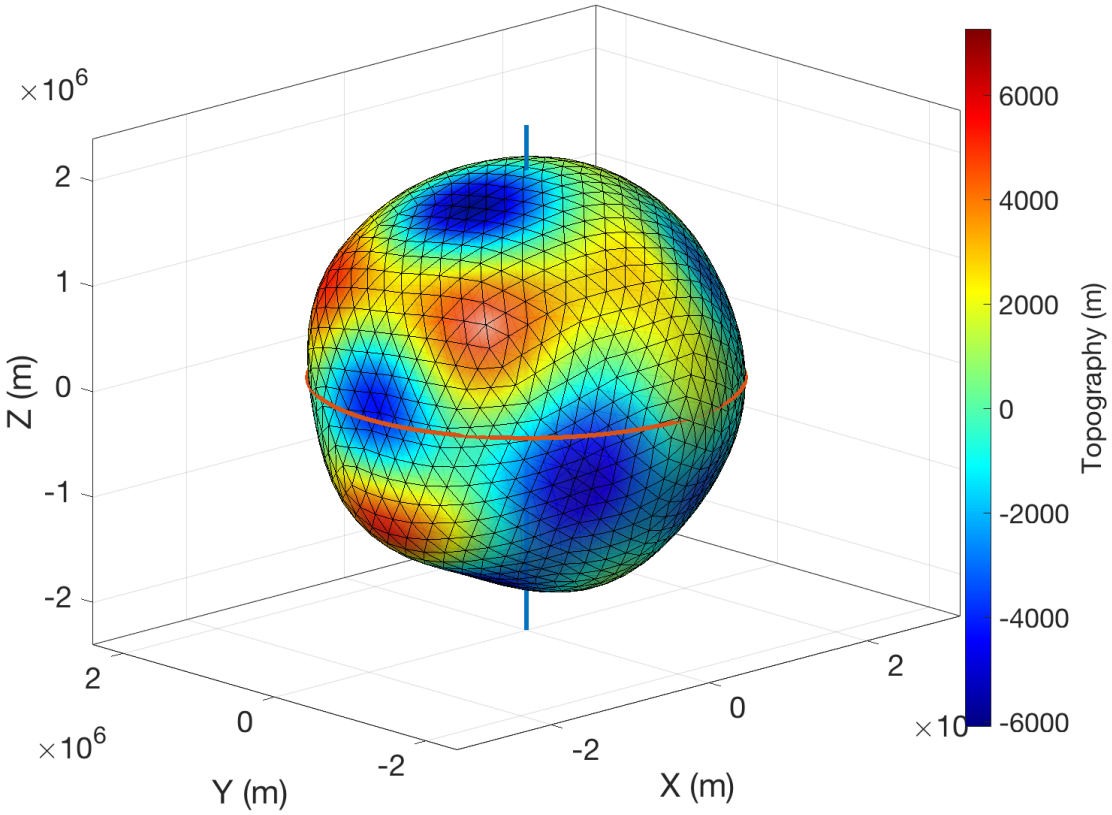

Figure 17. A model with topography (model-2) for the planet. I have exaggerated the plotting of the topography by 20 times. Colors indicate topography relative to the mean radius of the planet with size given in meters. The thick red line is the equator. The blue vertical thick line is the axis through the poles.

For model-2, I generate the surface topography for the planet using spherical harmonics up to and including order 6 (Figure 17) Specifically, the topography, h, is generated by the summation of spherical harmonics, $h(\theta,\phi) = \sum_{l=0}^{6}\sum_{m=-l}^{l} c_{lm} Y_l^m(\theta,\phi)$, where h is the height of the topography from the reference sphere, θ and ϕ are the angular positions on the surface, and Y_l^m represents the fully normalized spherical harmonics. I generate random numbers for the coefficients, c_{lm} to construct the topography for model-2. I use the same numerical procedure laid out in Section 3.1 to compute the seismic wavefield for model-2, along with the torque on the moon and the orbital decay rate of the moon. To see the

topography effect on the tidal seismic resonance, I take the derivative of the orbital decay rate with respect to the orbital radius and several localized changes at some radii show up (Figure 18a). These changes are caused by topography induced tidal-seismic resonance. To validate this claim, I run a seismic wavefield modeling using the two models (model-1 and model-2) and obtain histories of orbital decay rates for both models. I then calculate the derivative of the orbital decay rate with respect to the orbital radius for the two models (Figure 18 a &b). I observe localized changes for the topography model, model-2 (Figure 18a). In contrast, I observe a smooth curve (no localized changes) for the orbital decay rate derivative using model-1 with no topography (Figure 18b). Hence, topography can indeed induce tidal-seismic resonance at higher orbits.

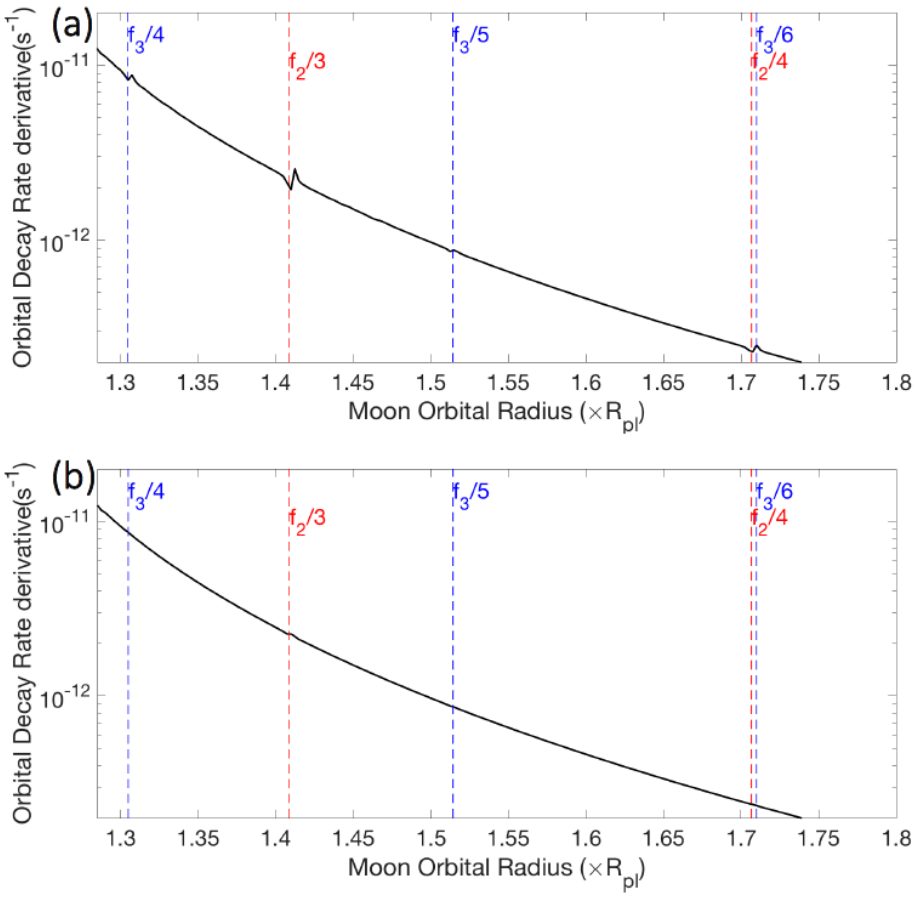

Figure 18. The derivative of the orbital decay rate with respect to the orbital radius for (a) model-2 with topography and (b) model-1 with no topography. Here, f_n is the frequency of

the normal mode ${}_0S_n$. A dashed line shows the orbit whose orbital frequency is f_n/m, where n and m are integers and labeled accordingly next to the dashed line. The radius of the planet R_{pl} is 2×10^6 m.

6.4 Mars-Phobos system

Tidal forces play an important role in the orbital evolution of the Martian moon, Phobos (Black and Mittal, 2015; Hesselbrock and Minton, 2017) because Phobos is below the synchronous orbit. Phobos is spiraling towards Mars because of tidal torque. Will the proposed tidal-seismic resonance effect play a role in this system? Presently, Phobos' orbit radius is about 2.77 times the Mars radius (Rm), which is too far to induce a significant tidal-seismic resonance. However, when Phobos' orbit decays to about $1.97 \times Rm$, the topography induced tidal-seismic resonance will occur, provided Phobos is strong enough and is not fragmented by Mars gravity field at the Roche limit. The strength of Phobos depends on the internal friction angle of the material in Phobos. The Roche limit of $1.97 \times Rm$ orbit corresponds to an internal friction angle of 40° (Holsapple and Michel, 2006). If the angle is larger than 40° (Holsapple and Michel, 2006) or a stronger Phobos, the tidal seismic resonance can occur before Phobos reaches the Roche limit. When Phobos' orbit is at $1.97 \times Rm$, I estimate the orbital decay rate to be about $10^{-10}\ m/s$ based on the present-day Martian topography using an approximate homogenous Mars model (P-wave velocity $v_p = 7.4\ km/s$, S-wave velocity $v_s = 3.6\ km/s$, density $\rho = 4000\ kg/m^3$ to match a ${}_0S_2$ period of about 2300 s (Zheng *et al.*, 2015). This rate is about 8% of the current orbital decay rate of Phobos, which is approximately $1.28 \times 10^{-9}\ m/s$ (Bills *et al.*, 2005). As Phobos continues falling towards Mars, the effect of tidal-seismic resonance will be more and more powerful in pulling Phobos towards Mars. Because of the tidal-seismic resonance, I note that Phobos

cannot stay at low orbits for a long time even if it is below the Roche limit and not fragmented.

6.5 Summary

The tidal-seismic resonance effect can be important in understanding planet-moon evolution if the moon is below the synchronous orbit. Planet topography can excite tidal-seismic resonance even if the moon is far away from the planet. The tidal seismic resonance can result in a large negative torque on the orbiting moon, which can increase the orbital decay rate of the moon toward the planet it is orbiting by one order of magnitude. It is also conceivable that the tidal-seismic resonance may also significantly accelerate the planetary accretion and formation process. The tidal-seismic phenomenon may also provide us with a potential method for interrogating the structure and compositional information of a planet without having to land an instrument on its surface. By precisely measuring the orbital decay rate as a function of radii, we can infer the normal mode frequencies of the planet, which can convey a wealth of information about the planet's interior.

Appendix

Analytical non self-gravitation Love number calculation Mathematica script

```
In[•]:= ClearAll["Global`*"]

In[•]:= subs1 = {Y^(2,0)[θ, ϕ] → -Csc[θ]^2 Y^(0,2)[θ, ϕ] - Cot[θ] Y^(1,0)[θ, ϕ] - L Y[θ, ϕ]}
        subs2 = {Y^(0,1)[θ, ϕ] → I m Y[θ, ϕ], Y^(1,1)[θ, ϕ] → I m Y^(1,0)[θ, ϕ]}
        subs3 = {Y^(0,2)[θ, ϕ] → - m m Y[θ, ϕ], Y^(1,2)[θ, ϕ] → - m m Y^(1,0)[θ, ϕ]}

Out[•]= {Y^(2,0)[θ, ϕ] → -L Y[θ, ϕ] - Csc[θ]^2 Y^(0,2)[θ, ϕ] - Cot[θ] Y^(1,0)[θ, ϕ]}

Out[•]= {Y^(0,1)[θ, ϕ] → i m Y[θ, ϕ], Y^(1,1)[θ, ϕ] → i m Y^(1,0)[θ, ϕ]}

Out[•]= {Y^(0,2)[θ, ϕ] → -m^2 Y[θ, ϕ], Y^(1,2)[θ, ϕ] → -m^2 Y^(1,0)[θ, ϕ]}

In[•]:= vecR[r_, θ_, ϕ_] := U[r] {Y[θ, ϕ], 0, 0}
        vecS[r_, θ_, ϕ_] := V[r] {0, D[Y[θ, ϕ], θ], 1 / Sin[θ] D[Y[θ, ϕ], ϕ]} / Sqrt[L]
        vecT[r_, θ_, ϕ_] := W[r] {0, 1 / Sin[θ] D[Y[θ, ϕ], ϕ], -D[Y[θ, ϕ], θ]} / Sqrt[L]

In[•]:= (* strain *)
        u = vecR[r, θ, ϕ] + vecS[r, θ, ϕ] (*+vecT[r,θ,ϕ]*)

Out[•]= {U[r] × Y[θ, ϕ], V[r] Y^(1,0)[θ, ϕ] / √L, Csc[θ] V[r] Y^(0,1)[θ, ϕ] / √L}

In[•]:= u_r = u[[1]]; (* radial displ *)
        u_θ = u[[2]] ; (* theta displ *)
        u_ϕ = u[[3]];
        (* phi displ *)

In[•]:= (* compute strain tensors *)
        e_rr = D[u_r, {r}];
        e_θθ = D[u_θ, {θ}] / r + u_r / r;
        e_ϕϕ = D[u_ϕ, {ϕ}] / (r Sin[θ]) + 1 / r u_θ Cot[θ] + u_r / r;
        e_rθ = D[u_θ, {r}] - u_θ / r + D[u_r, {θ}] / r;
        e_rϕ = D[u_r, {ϕ}] / (r Sin[θ]) + D[u_ϕ, {r}] - u_ϕ / r;
        e_θϕ = D[u_ϕ, {θ}] / r - u_ϕ Cot[θ] / r + D[u_θ, {ϕ}] / r / Sin[θ];

In[•]:= λ = B μ

Out[•]= B μ
```

```
In[•]:= F0 = λ
        L0 = μ
        N0 = μ
        A0 = λ + 2 μ
        C0 = λ + 2 μ
```

Out[•]= B μ

Out[•]= μ

Out[•]= μ

Out[•]= 2 μ + B μ

Out[•]= 2 μ + B μ

```
In[•]:= (* compute stress tensors *)
        σrr = C0 err + F0 (eθθ + eϕϕ);
        σrr = σrr /. subs1 /. subs2 /. subs3 // Simplify;
        σθθ = F0 err + A0 (eθθ + eϕϕ) - 2 N0 eϕϕ;
        σθθ = σθθ /. subs1 /. subs2 /. subs3 // Simplify;
        σϕϕ = F0 err + A0 (eθθ + eϕϕ) - 2 N0 eθθ ;
        σϕϕ = σϕϕ /. subs1 /. subs2 /. subs3 // Simplify;
        σrθ = L0 erθ ; σrθ = σrθ /. subs1 /. subs2 /. subs3 // Simplify;
        σrϕ = L0 erϕ ; σrϕ = σrϕ /. subs1 /. subs2 /. subs3 // Simplify;
        σθϕ = N0 eθϕ;
         σθϕ = σθϕ /. subs1 /. subs2 /. subs3 // Simplify;;
In[•]:= (* equations of motion *)


        compr = (*ρ ω^2 ur *) + D[σrr, {r}] + 1 / r D[σrθ, {θ}] + 1 / (r Sin[θ]) D[σrϕ, {ϕ}] +
           1 / r (2 σrr - σθθ - σϕϕ + Cot[θ] σrθ);
        compt = (*ρ ω^2 uθ*) + D[σrθ, {r}] + 1 / r D[σθθ, {θ}] + 1 / (r Sin[θ]) D[σθϕ, {ϕ}] +
           1 / r (3 σrθ + (σθθ - σϕϕ) Cot[θ] );
        compp = (*ρ ω^2 uϕ *) + D[σrϕ, {r}] + 1 / r D[σθϕ, {θ}] + 1 / (r Sin[θ]) D[σϕϕ, {ϕ}] +
           1 / r (3 σrϕ + 2 σθϕ Cot[θ] );

In[•]:= eq1 = compr /. subs1 /. subs2 /. subs3 // FullSimplify
        eq2 = compt /. subs1 /. subs2 /. subs3 // FullSimplify
        eq3 = compp /. subs1 /. subs2 /. subs3 // FullSimplify
```

Out[•]= $\frac{1}{r^2}\mu\, Y[\theta,\phi]\left(-(4+2B+L)\,U[r]+(3+B)\sqrt{L}\,V[r]+r\left(2(2+B)\,U'[r]-(1+B)\sqrt{L}\,V'[r]+(2+B)\,r\,U''[r]\right)\right)$

Out[•]= $\frac{1}{\sqrt{L}\,r^2}\mu\left(2(2+B)\sqrt{L}\,U[r]-(2+B)\,L\,V[r]+r\left((1+B)\sqrt{L}\,U'[r]+2V'[r]+r\,V''[r]\right)\right)Y^{(1,0)}[\theta,\phi]$

Out[•]= $-\frac{1}{\sqrt{L}\,r^2}i\,m\,\mu\,\mathrm{Csc}[\theta]\,Y[\theta,\phi]\left(-2(2+B)\sqrt{L}\,U[r]+(2+B)\,L\,V[r]-r\left((1+B)\sqrt{L}\,U'[r]+2V'[r]+r\,V''[r]\right)\right)$

In[•]:= l = 2

Out[•]= 2

In[•]:= (* tidal force *)

In[•]:= Vtidal = A r^2 Y[θ, ϕ]

Out[•]= A r^2 Y[θ, ϕ]

In[•]:= force1 = rho D[Vtidal, r]

Out[•]= 2 A r rho Y[θ, ϕ]

In[•]:= force2 = rho D[Vtidal, θ] / r

Out[•]= A r rho Y^(1,0)[θ, ϕ]

In[•]:= force3 = rho D[Vtidal, ϕ] / (r Sin[θ])

Out[•]= A r rho Csc[θ] Y^(0,1)[θ, ϕ]

In[•]:= fac = Sqrt[5 / 4 / Pi]

Out[•]= $\frac{\sqrt{\frac{5}{\pi}}}{2}$

In[•]:= eq11 = (force1 + eq1) / Y[θ, ϕ] // Simplify

Out[•]= $\frac{1}{r^2}\left(-(4+2B+L)\,\mu\,U[r] + (3+B)\sqrt{L}\,\mu\,V[r] + r\left(2(2+B)\,\mu\,U'[r] - (1+B)\sqrt{L}\,\mu\,V'[r] + r\left(2A\,r\,rho + (2+B)\,\mu\,U''[r]\right)\right)\right)$

In[•]:= eq22 = (eq2 + force2) / Y^(1,0)[θ, ϕ] // Simplify

Out[•]= $\frac{1}{\sqrt{L}\,r^2}\left(2(2+B)\sqrt{L}\,\mu\,U[r] - (2+B)\,L\,\mu\,V[r] + r\left(A\sqrt{L}\,r^2\,rho + (1+B)\sqrt{L}\,\mu\,U'[r] + 2\,\mu\,V'[r] + r\,\mu\,V''[r]\right)\right)$

In[•]:= eq3 /. {m → 0}

Out[•]= 0

In[•]:= σrr

Out[•]= $\frac{\mu\,Y[\theta,\phi]\left(2B\,U[r] - B\sqrt{L}\,V[r] + (2+B)\,r\,U'[r]\right)}{r}$

In[•]:= Trr = σrr / Y[θ, ϕ]

Out[•]= $\frac{\mu\left(2B\,U[r] - B\sqrt{L}\,V[r] + (2+B)\,r\,U'[r]\right)}{r}$

In[•]:= Trtheta = σrθ / Y^(1,0)[θ, ϕ]

Out[•]= $\frac{\mu\left(\sqrt{L}\,U[r] - V[r] + r\,V'[r]\right)}{\sqrt{L}\,r}$

```
In[•]:= Vs = 1200; Vp = 6000; rho = 2840;
        mu = rho * Vs^2 ;
        lambda = rho * Vp^2 - 2 * mu ;

In[•]:= ra = 2 000 000 (* planet radius *)

Out[•]= 2 000 000

In[•]:= moon = 10^16 (*moon mass*)

Out[•]= 10 000 000 000 000 000

In[•]:= rp  = 10 ra

Out[•]= 20 000 000

In[•]:= Mplanet = 4 / 3 * Pi * ra^3 * rho

Out[•]= 90 880 000 000 000 000 000 000 π
                                        3

In[•]:= G = 6.67408 × 10^(-11)

Out[•]= 6.67408 × 10^-11

In[•]:= gplanet = G Mplanet / ra^2

Out[•]= 1.58792

In[•]:= Anum = G * moon / rp^3 / fac

Out[•]= 1.32258 × 10^-16

In[•]:= sub10 = {λ → lambda, μ → mu, A → Anum}

Out[•]= {B μ → 94 060 800 000, μ → 4 089 600 000, A → 1.32258 × 10^-16}

In[•]:= eq11

Out[•]= 1/r^2 (-(4 + 2 B + L) μ U[r] + (3 + B) √L μ V[r] +
          r (2 (2 + B) μ U'[r] - (1 + B) √L μ V'[r] + r (5680 A r + (2 + B) μ U''[r])))

In[•]:= eq22

Out[•]= 1/(√L r^2) (2 (2 + B) √L μ U[r] - (2 + B) L μ V[r] +
          r (2840 A √L r^2 + (1 + B) √L μ U'[r] + 2 μ V'[r] + r μ V''[r]))

In[•]:= eqns = {eq11 == 0, eq22 == 0}

Out[•]= {1/r^2 (-(4 + 2 B + L) μ U[r] + (3 + B) √L μ V[r] +
            r (2 (2 + B) μ U'[r] - (1 + B) √L μ V'[r] + r (5680 A r + (2 + B) μ U''[r]))) == 0,
         1/(√L r^2) (2 (2 + B) √L μ U[r] - (2 + B) L μ V[r] +
            r (2840 A √L r^2 + (1 + B) √L μ U'[r] + 2 μ V'[r] + r μ V''[r])) == 0}
```

In[•]:=
```
DSolve[eqns, {U, V}, r] // Simplify
```

Out[•]=
$$\text{DSolve}\left[\left\{\frac{1}{r}\left(-(4+2\,B+L)\,\mu\,U[r]+(3+B)\,\sqrt{L}\,\mu\,V[r]+r\left(2\,(2+B)\,\mu\,U'[r]-(1+B)\,\sqrt{L}\,\mu\,V'[r]+r\left(5680\,A\,r+(2+B)\,\mu\,U''[r]\right)\right)\right)==0,\ \frac{1}{\sqrt{L}\,r^2}\left(2\,(2+B)\,\sqrt{L}\,\mu\,U[r]-(2+B)\,L\,\mu\,V[r]+r\left(2840\,A\,\sqrt{L}\,r^2+(1+B)\,\sqrt{L}\,\mu\,U'[r]+2\,\mu\,V'[r]+r\,\mu\,V''[r]\right)\right)==0\right\},\{U,V\},r\right]$$

In[•]:=
```
Ur = -568 A (10 + 3 B) r^3/(7 (2 + B) μ) + r C3 + r^3 C4
```

Out[•]=
$$C3\,r+C4\,r^3-\frac{568\,A\,(10+3\,B)\,r^3}{7\,(2+B)\,\mu}$$

In[•]:=
```
Vr = -284 Sqrt[6] A (12 + 5 B) r^3/(7 (2 + B) μ) + Sqrt[3/2] r C3 + (7 Sqrt[6] + 5 Sqrt[6] B) r^3 C4/(6 B)
```

Out[•]=
$$\sqrt{\frac{3}{2}}\,C3\,r+\frac{\left(7\sqrt{6}+5\sqrt{6}\,B\right)C4\,r^3}{6\,B}-\frac{284\sqrt{6}\,A\,(12+5\,B)\,r^3}{7\,(2+B)\,\mu}$$

In[•]:=
```
Trr
```

Out[•]=
$$\frac{\mu\left(2\,B\,U[r]-B\sqrt{L}\,V[r]+(2+B)\,r\,U'[r]\right)}{r}$$

In[•]:=
```
Trrsurface = (2 Sqrt[6] B Ur - 6 B Vr + Sqrt[6] (2 + B) r D[Ur, r]) /. {r → a} // Simplify
```

Out[•]=
$$\frac{1}{7}\sqrt{6}\,a\left(14\,C3+a^2\left(-7\,C4-\frac{2272\,A\,(15+8\,B)}{(2+B)\,\mu}\right)\right)$$

In[•]:=
```
Trtheta
```

Out[•]=
$$\frac{\mu\left(\sqrt{L}\,U[r]-V[r]+r\,V'[r]\right)}{\sqrt{L}\,r}$$

In[•]:=
```
Trthetasurface = (Sqrt[6] Ur - Vr + r D[Vr, r]) /. {r → a} // Simplify
```

Out[•]=
$$\frac{1}{7}\sqrt{\frac{2}{3}}\,a\left(21\,C3+\frac{a^2\left(-3408\,A\,B\,(11+4\,B)+7\left(14+23\,B+8\,B^2\right)C4\,\mu\right)}{B\,(2+B)\,\mu}\right)$$

In[•]:=
```
sol = Solve[{Trrsurface == 0, Trthetasurface == 0}, {C3, C4}]
```

Out[•]=
$$\left\{\left\{C3\to\frac{5680\,a^2\,A\,(3+4\,B)}{(14+19\,B)\,\mu},\ C4\to-\frac{27\,264\,\left(A\,B+A\,B^2\right)}{7\,(2+B)\,(14+19\,B)\,\mu}\right\}\right\}$$

In[•]:= C3 = C3 /. sol[[1]]

Out[•]= $\frac{5680\, a^2\, A\, (3 + 4\, B)}{(14 + 19\, B)\, \mu}$

In[•]:= C4 = C4 /. sol[[1]]

Out[•]= $-\frac{27\,264\, \left(A\, B + A\, B^2\right)}{7\, (2 + B)\, (14 + 19\, B)\, \mu}$

In[•]:= a = ra

Out[•]= 2 000 000

In[•]:= A = Anum

Out[•]= 1.32258×10^{-16}

In[•]:= B = lambda / mu

Out[•]= 23

In[•]:= μ = mu

Out[•]= 4 089 600 000

In[•]:= C3

Out[•]= 1.54773×10^{-10}

In[•]:= C4

Out[•]= -6.16672×10^{-24}

In[•]:= Ura = Ur /. {r → a}

Out[•]= 0.000193874

In[•]:= Vra = Vr /. {r → a}

Out[•]= 0.000141669

In[•]:= Vnorthpole = G moon / rp ^ 3 a ^ 2

Out[•]= 0.000333704

In[•]:= hhydro = Vnorthpole / gplanet

Out[•]= 0.000210152

In[•]:= h2 = Ura / hhydro

Out[•]= 0.922542

In[•]:= (* hydrostatic tidal height;
verification with another experession below *)

In[•]:= h2 * fac // N

Out[•]= 0.581924

Bibliography

Aggarwal, H. R., and V. R. Oberbeck (1974), ROCHE LIMIT OF A SOLID BODY, *Astrophysical Journal*, ***191***(2), 577-588.

Aki, K., and P. G. Richards (2002), *Quantitative seismology*.

Arakawa, M., et al. (2020), An artificial impact on the asteroid (162173) Ryugu formed a crater in the gravity-dominated regime, *Science*, ***368***(6486), 67.

Asphaug, E., and W. Benz (1994), Density of Comet Shoemaker-Levy-9 Deduced by Modeling Breakup of the Parent Rubble-Pile, *Nature*, ***370***(6485), 120-124.

Asphaug, E., J. M. Moore, D. Morrison, W. Benz, M. C. Nolan, and R. J. Sullivan (1996), Mechanical and Geological Effects of Impact Cratering on Ida, *Icarus*, ***120***(1), 158-184.

Banerdt, W. B., et al. (2020), Initial results from the InSight mission on Mars, *Nature Geoscience*.

Barker, A. J., H. J. Braviner, and G. I. Ogilvie (2016), Non-linear tides in a homogeneous rotating planet or star: global modes and elliptical instability, *Monthly Notices of the Royal Astronomical Society*, ***459***(1), 924-938.

Ben-Menahem, A., and S. J. Singh (1981), Seismic waves and sources, edited, Springer-Verlag New York Inc.

Ben-Menahem, A., and S. J. Singh (2012), *Seismic waves and sources*, Springer Science & Business Media.

Bills, B. G., G. A. Neumann, D. E. Smith, and M. T. Zuber (2005), Improved estimate of tidal dissipation within Mars from MOLA observations of the shadow of Phobos, *Journal of Geophysical Research-Planets*, ***110***(E7).

Black, B. A., and T. Mittal (2015), The demise of Phobos and development of a Martian ring system, *Nature Geoscience*, ***8***(12), 913-U936.

Boore, D. M. (1972), Finite difference methods for seismic wave propagation in heterogeneous materials, *Methods in computational physics*, ***11***, 1-37.

Bouchon, M., M. Campillo, and S. Gaffet (1989), A boundary integral equation-discrete wavenumber representation method to study wave propagation in multilayered media having irregular interfaces, *Geophysics*, ***54***(9), 1134-1140.

Braviner, H. J., and G. I. Ogilvie (2014a), Tidal interactions of a Maclaurin spheroid–I. Properties of free oscillation modes, *Monthly Notices of the Royal Astronomical Society*, ***441***(3), 2321-2345.

Braviner, H. J., and G. I. Ogilvie (2014b), Tidal interactions of a Maclaurin spheroid–II. Resonant excitation of modes by a close, misaligned orbit, *Monthly Notices of the Royal Astronomical Society*, ***447***(2), 1141-1153.

Chaillat, S., M. Bonnet, and J.-F. Semblat (2009), A new fast multi-domain BEM to model seismic wave propagation and amplification in 3-D geological structures, *Geophysical Journal International*, ***177***(2), 509-531.

Chen, J. J., and D. Kipping (2017), PROBABILISTIC FORECASTING OF THE MASSES AND RADII OF OTHER WORLDS, *Astrophysical Journal*, ***834***(1).

Cummins, P. R., R. J. Geller, T. Hatori, and N. Takeuchi (1994a), DSM complete synthetic seismograms: SH, spherically symmetric, case, *Geophysical Research Letters*, ***21***(7), 533-536.

Cummins, P. R., R. J. Geller, and N. Takeuchi (1994b), DSM complete synthetic seismograms: P-SV, spherically symmetric, case, *Geophysical Research Letters*, ***21***(15), 1663-1666.

Dahlen, F. A., and J. Tromp (1998), *Theoretical Global Seismology*, Princeton University Press, Princeton, New Jersey.

Darwin, G. H. (1898a), The evolution of satellites, *The Atlantic Monthly*, ***81***, 444-455.

Darwin, G. H. (1898b), The tides and kindred phenomena in the solar system, *Boston and New York*.

DellaGiustina, D. N., et al. (2019), Properties of rubble-pile asteroid (101955) Bennu from OSIRIS-REx imaging and thermal analysis, *Nature Astronomy*, ***3***(4), 341-351.

Fang, X., M. C. Fehler, and A. Cheng (2014), Simulation of the effect of stress-induced anisotropy on borehole compressional wave propagation, *Geophysics*, ***79***(4), D205-D216.

Fuller, J. (2014), Saturn ring seismology: Evidence for stable stratification in the deep interior of Saturn, *Icarus*, ***242***, 283-296.

Fuller, J., J. Luan, and E. Quataert (2016), Resonance locking as the source of rapid tidal migration in the Jupiter and Saturn moon systems, *Monthly Notices of the Royal Astronomical Society*, ***458***(4), 3867-3879.

Ge, Z., and X. Chen (2008), An Efficient Approach for Simulating Wave Propagation with the Boundary Element Method in Multilayered Media with Irregular Interfaces, *Bulletin of the Seismological Society of America*, ***98***(6), 3007-3016.

Ge, Z., L.-Y. Fu, and R.-S. Wu (2005), P-SV wave-field connection technique for regional wave propagation simulation, *Bulletin of the Seismological Society of America*, ***95***(4), 1375-1386.

Geller, R. J., and T. Ohminato (1994), Computation of synthetic seismograms and their partial derivatives for heterogeneous media with arbitrary natural boundary conditions using the Direct Solution Method, *Geophysical Journal International*, ***116***(2), 421-446.

Geller, R. J., and N. Takeuchi (1995), A new method for computing highly accurate DSM synthetic seismograms, *Geophysical Journal International*, ***123***(2), 449-470.

Giardini, D., et al. (2020), The seismicity of Mars, *Nature Geoscience*.

Hesselbrock, A. J., and D. A. Minton (2017), An ongoing satellite–ring cycle of Mars and the origins of Phobos and Deimos, *Nature Geoscience*, ***10***, 266.

Holsapple, K. A., and P. Michel (2006), Tidal disruptions: A continuum theory for solid bodies, *Icarus*, ***183***(2), 331-348.

Johansen, A., E. Jacquet, J. N. Cuzzi, A. Morbidelli, and M. Gounelle (2015), New Paradigms for Asteroid Formation, in *Asteroids IV*, edited by Michel et al., pp. 471-492, University of Arizona, Tucson.

Kawai, K., N. Takeuchi, and R. J. Geller (2006), Complete synthetic seismograms up to 2 Hz for transversely isotropic spherically symmetric media, *Geophysical Journal International*, ***164***(2), 411-424.

Komatitsch, D., and J. Tromp (1999), Introduction to the spectral element method for three-dimensional seismic wave propagation, *Geophysical Journal International*, ***139***(3), 806-822.

Lognonné, P., et al. (2020), Constraints on the shallow elastic and anelastic structure of Mars from InSight seismic data, *Nature Geoscience*.

Lognonné, P., D. Giardini, B. Banerdt, J. Gagnepain-Beyneix, A. Mocquet, T. Spohn, J. Karczewski, P. Schibler, S. Cacho, and W. Pike (2000), The NetLander very broad band seismometer, *Planetary and Space Science*, ***48***(12-14), 1289-1302.

Love, A. E. H. (1911), *Some problems of geodynamics*, University Press in Cambridge.

Lu, J. N., Y. S. Sun, M. N. Toksoz, Y. C. Zheng, and M. T. Zuber (2011), Seismic effects of the Caloris basin impact, Mercury, *Planetary and Space Science*, ***59***(15), 1981-1991.

Marley, M. S. (1991), Nonradial oscillations of Saturn, *Icarus*, ***94***(2), 420-435.

Marley, M. S. (2014), Saturn ring seismology: Looking beyond first order resonances, *Icarus*, ***234***, 194-199.

Marley, M. S., and C. C. Porco (1993), Planetary acoustic mode seismology: Saturn's rings, *Icarus*, ***106***(2), 508-524.

Masters, G., J. Woodhouse, and G. Freeman (2011), Mineos v1. 0.2 [software], Computational Infrastructure for Geodynamics, edited.

Murdoch, N., S. Hempel, L. Pou, A. Cadu, R. F. Garcia, D. Mimoun, L. Margerin, and O. Karatekin (2017), Probing the internal structure of the asteriod Didymoon with a passive seismic investigation, *Planetary and Space Science*, ***144***, 89-105.

Murray, C. D., and S. F. Dermott (1999), *Solar system dynamics*, Cambridge university press.

Nimmo, F., and U. H. Faul (2013), Dissipation at tidal and seismic frequencies in a melt-free, anhydrous Mars, *Journal of Geophysical Research-Planets*, ***118***(12), 2558-2569.

Nimmo, F., J. R. Spencer, R. T. Pappalardo, and M. E. Mullen (2007), Shear heating as the origin of the plumes and heat flux on Enceladus, *Nature*, ***447***(7142), 289-291.

Sánchez-Sesma, F. J., and M. Campillo (1991), Diffraction of P, SV, and Rayleigh waves by topographic features: A boundary integral formulation, *Bulletin of the Seismological Society of America*, ***81***(6), 2234-2253.

Schultz, P. H., and D. E. Gault (1975), Seismic effects from major basin formations on the moon and Mercury, *The Moon*, ***12***, 159-177.

Semechko, A. (2015), Suite of functions to perform uniform sampling of a sphere, *MATLAB File Exchange Server*.

Stamos, A., and D. Beskos (1996), 3-D seismic response analysis of long lined tunnels in half-space, *Soil Dynamics and Earthquake Engineering*, ***15***(2), 111-118.

Takeuchi, N., R. J. Geller, and P. R. Cummins (1996), Highly accurate P - SV complete synthetic seismograms using modified DSM operators, *Geophysical Research Letters*, ***23***(10), 1175-1178.

Taylor, P. A., and J. L. Margot (2010), Tidal evolution of close binary asteroid systems, *Celestial Mechanics & Dynamical Astronomy*, ***108***(4), 315-338.

Tian, Y., and Y. Zheng (2019), Rapid falling of an orbiting moon to its parent planet due to tidal-seismic resonance, *Planetary and Space Science*, 104796.

Walsh, K. J. (2018), Rubble Pile Asteroids, *Annual Review of Astronomy and Astrophysics*, ***56***(1), 593-624.

Willner, K., X. Shi, and J. Oberst (2014), Phobos' shape and topography models, *Planetary and Space Science*, ***102***, 51-59.

Xiao, H., and Z. Gimbutas (2010), A numerical algorithm for the construction of efficient quadrature rules in two and higher dimensions, *Computers & mathematics with applications*, ***59***(2), 663-676.

Zhan, X., X. Fang, R. Daneshvar, E. Liu, and C. E. Harris (2014), Full elastic finite-difference modeling and interpretation of karst system in a subsalt carbonate reservoir, *Interpretation*, ***2***(1), T49-T56.

Zhang, W., Z. Zhang, and X. Chen (2012), Three-dimensional elastic wave numerical modelling in the presence of surface topography by a collocated-grid finite-difference method on curvilinear grids, *Geophysical Journal International*, ***190***(1), 358-378.

Zharkov, V., and T. Gudkova (1997), On the dissipative factor of the Martian interiors, *Planetary and Space Science*, ***45***(4), 401-407.

Zheng, Y., A. Malallah, M. Fehler, and H. Hu (2016), 2D full-waveform modeling of seismic waves in layered karstic media, *Geophysics*, ***81***(2), T25-T34.

Zheng, Y., F. Nimmo, and T. Lay (2015), Seismological implications of a lithospheric low seismic velocity zone in Mars, *Physics of the Earth and Planetary Interiors*, ***240***, 132-141.